The Astrophysical Journal, 945:127 (16pp), 2023 March 10 https://doi.org/10.3847/1538-4357/acb772

A Catalog of 71 Coronal Line Galaxies in MaNGA: [Ne V] Is an Effective AGN Tracer

James Negus[1], Julia M. Comerford[1], Francisco Müller Sánchez[2], Mitchell Revalski[3], Rogemar A. Riffel[4,5], Kevin Bundy[6], Rebecca Nevin[7], and Sandro B. Rembold[4,5]
[1] Department of Astrophysical and Planetary Sciences, University of Colorado, Boulder, CO 80309, USA; james.negus@colorado.edu
[2] Department of Physics, The University of Memphis, Memphis, TN 38152, USA
[3] Space Telescope Science Institute, 3700 San Martin Drive, Baltimore, MD 21218, USA
[4] Departamento de Física, CCNE, Universidade Federal de Santa Maria, 97105-900, Santa Maria, RS, Brazil
[5] Laboratório Interinstitucional de e-Astronomia—LIneA, Rua Gal. José Cristino 77, Rio de Janeiro, RJ—20921-400, Brazil
[6] UCO/Lick Observatory, Department of Astronomy and Astrophysics, University of California, 1156 High Street, Santa Cruz, CA 95064, USA
[7] Fermi National Accelerator Laboratory, Batavia, IL 60510, USA
Received 2022 October 21; revised 2023 January 23; accepted 2023 January 29; published 2023 March 14

Abstract

Despite the importance of active galactic nuclei (AGNs) in galaxy evolution, accurate AGN identification is often challenging, as common AGN diagnostics can be confused by contributions from star formation and other effects (e.g., Baldwin–Phillips–Terlevich diagrams). However, one promising avenue for identifying AGNs is "coronal emission lines" ("CLs"), which are highly ionized species of gas with ionization potentials $\geqslant$100 eV. These CLs may serve as excellent signatures for the strong ionizing continuum of AGNs. To determine if CLs are in fact strong AGN tracers, we assemble and analyze the largest catalog of optical CL galaxies using the Sloan Digital Sky Survey's Mapping Nearby Galaxies at Apache Point Observatory (MaNGA) catalog. We detect CL emission in 71 MaNGA galaxies, out of the 10,010 unique galaxies from the final MaNGA catalog, with $\geqslant 5\sigma$ confidence. In our sample, we measure [Ne V]λ3347, λ3427, [Fe VII]λ3586, λ3760, λ6086, and [Fe X]λ6374 emission and crossmatch the CL galaxies with a catalog of AGNs that were confirmed with broad-line, X-ray, IR, and radio observations. We find that [Ne V] emission, compared to [Fe VII] and [Fe X] emission, is best at identifying high-luminosity AGNs. Moreover, we find that the CL galaxies with the least dust extinction yield the most iron CL detections. We posit that the bulk of the iron CLs are destroyed by dust grains in the galaxies with the highest [O III] luminosities in our sample, and that AGNs in the galaxies with low [O III] luminosities are possibly too weak to be detected using traditional techniques.

Unified Astronomy Thesaurus concepts: Active galactic nuclei (16); Photoionization (2060); Emission line galaxies (459); Astrophysical dust processes (99)

1. Introduction

Active galactic nucleus (AGN) feedback, the process by which an active accretion disk converts gravitational energy into radiative or mechanical energy (e.g., AGN-induced photoionization, outflows, shocks, winds, and jets), has been shown to dynamically influence the evolution of a host galaxy (e.g., the tight correlation between stellar velocity dispersion and black hole mass and the quenching of star formation; e.g., Ferrarese & Merritt 2000; Gebhardt et al. 2000; Di Matteo et al. 2005; Hopkins et al. 2005; Fabian 2012; Kormendy & Ho 2013; Heckman & Best 2014). However, the full spatial extent, ionization properties, and impact of AGN feedback on the host galaxy have yet to be fully unraveled.

The Unified Model of AGNs (Antonucci 1993; Urry & Padovani 1995) provides a fundamental architecture for understanding the evolution of AGN feedback. In this model, an AGN is either Type I or Type II. Type I are viewed pole-on and are observed to have broad (FWHM $\gtrapprox$ 1000 km s^{-1}) and narrow (FWHM $\lessapprox$ 1000 km s^{-1}) emission lines, whereas Type II are viewed edge-on and are observed to only have narrow emission lines. These regions are termed the broad-line region (BLR) and the narrow-line region (NLR), respectively.

In Negus et al. (2021), we considered the Unified Model before investigating the "coronal line region" (CLR), an area surrounding a supermassive black hole (SMBH; $M_{\rm BH} > 10^6$ $M_\odot$) that produces highly ionized species of gas with ionization potentials (IPs) $\gtrsim$ 100 eV (termed "coronal lines" (CLs) since they were first observed in the solar corona). CLs are suspected to primarily originate from the strong ionizing continuum of an AGN; in particular, nuclear CLs are produced in the inner edge of the dusty torus, and extended CLs are tied to the presence of a jet or AGN-driven outflows (due to the highly energetic nature of these processes; e.g., Rodríguez-Ardila et al. 2002, 2011; Almudena Prieto et al. 2005; Gelbord et al. 2009; Mullaney et al. 2009; Mazzalay et al. 2010; Müller-Sánchez et al. 2011; Glidden et al. 2016; Riffel et al. 2021; Trindade Falcão et al. 2022).

Further, CLs in the mid-infrared have been extensively used to probe for AGNs, and to subsequently analyze their physical environments, within dusty galaxies (e.g., Genzel et al. 1998; Sturm et al. 2002; Armus et al. 2004, 2023; Lutz et al. 2005; Weedman et al. 2006; Dasyra et al. 2008). In fact, several studies have shown that AGNs, even those missed by optical surveys (due to obscuration, for example), are uncovered by observations of infrared CLs (e.g., Satyapal et al. 2008, 2021; Sajina et al. 2022). Additionally, since CL emission from Type II supernovae is infrequent, weak, and short lived, CL infrared observations have been particularly useful for accurately identifying CL emission exclusively from AGNs (e.g., Smith et al. 2009).

In regard to optical studies, Baldwin–Phillips–Terlevich diagnostics diagrams (Baldwin et al. 1981; Veilleux & Osterbrock 1987; Kewley et al. 2001, 2006) are predominantly used to differentiate emission-line sources as star-forming, AGN, or a composite of the two. However, diffuse ionized gas, extraplanar gas, photoionization by hot stars, metallicity, and shocks can elevate sources beyond the star formation threshold and potentially lead to AGN misclassification (e.g., Wylezalek et al. 2018).

Moreover, while the NLR is the largest observable structure directly affected by an AGN's ionizing radiation (out to several kiloparsecs; e.g., Müller-Sánchez et al. 2011), star formation can also produce some of the narrow lines usually associated with AGNs (e.g., [O III] 5007; "[O III]" hereafter). Further, while the BLR provides definitive evidence of AGN activity, due to the elevated cloud velocities, its compact radial extent (≈0.1 kpc; e.g., Laor 2004) is spatially unresolved in most spectroscopic surveys. On the other hand, CLs require energies well above the limit of stellar emission (55 eV; Haehnelt et al. 2001) and are typically spatially resolved beyond the BLR and well into the NLR (e.g., Negus et al. 2021). If CLs can provide accurate AGN identification in optical spectroscopic surveys of galaxies, as they have been shown to do in infrared surveys, then detecting them may be a critical step in constraining the complexities of AGN feedback (e.g., Molina et al. 2021).

The Sloan Digital Sky Survey's (SDSS's) Mapping Nearby Galaxies at Apache Point Observatory catalog (MaNGA; Bundy et al. 2015) has provided an unprecedented lens into the dynamic environments that surround the SMBHs of nearly 10,010 nearby ($0.01 < z < 0.15$; average $z \approx 0.03$) galaxies. Using integral field spectroscopy (IFS), MaNGA provides a 1–2 kpc spatial sampling across the field of view (FOV) of each observed galaxy, which offers direct insight into the spatial extent, ionization properties, and the environmental impact of AGN feedback. For reference, previous SDSS surveys (e.g., SDSS-I to SDSS-III; York et al. 2000; Eisenstein et al. 2011) observed galaxies with small (3″ diameter) optical fibers. The resulting spectra only traced a small region close to the galactic center, potentially missing nuclear activity outside of this region. Yan et al. (2016) further reported that 80% of SDSS galaxies observed with a single fiber have less than 36% of their light covered. Moreover, long-slit spectroscopic surveys of galaxies also reveal limited spatial information, since only narrow elongated regions of each galaxy are observed (e.g., Newman et al. 2013). In contrast, MaNGA offers the ability to capture spatially extended galactic features, which can reveal off-nuclear activity and large-scale emission-line regions.

In Negus et al. (2021), we scanned for [Ne V]λ3347, λ3427, [Fe VII]λ3586, λ3760, λ6086, and [Fe X]λ6374 emission at $\geqslant 5\sigma$ above the background continuum in the 6623 galaxies from MaNGA's eighth data release (MPL-8). We identified 10 CL galaxies in MPL-8, the largest such catalog at the time; seven of which were confirmed to host an AGN, which suggests that CL emission can be useful for tracing AGN activity. The remaining three visually appear to be undergoing galactic mergers. We also found that the average spatial extent of the CLR from the nuclear center is 6.6 kpc—well into the NLR. Further, we measured the average electron number density of the CLRs in our sample to be on the order of $\approx 10^2$ cm^{-3}, also consistent with the CLR occupying the traditional NLR, beyond the BLR (typical NLR densities range from 10^1–10^7 cm^{-3}; e.g., Peterson 1997; Revalski et al. 2022).

However, we also reported a range of power-law indices above the threshold expected for pure AGN photoionization, and electron temperature values slightly above the threshold for pure AGN photoionization ($T_e = 20{,}000$ K; Osterbrock 1981). We found that the average CLR electron temperatures varied between 12,331 and 22,530 K. These results suggest that shock-induced compression and heating may also play a role in the production of CLs.

Comparatively, Mazzalay et al. (2010) investigated the CLR for 10 pre-selected AGNs. They used the Hubble Space Telescope (HST)/Space Telescope Imaging Spectrograph (STIS) to study [Ne V] λ3427, [Fe VII] λ3586, λ3760, λ6086, [Fe X] λ6374, [Fe XIV] λ5303, [Fe XI] λ7892, and [S XII] λ7611 emission in their sample. The authors deduced that AGN photoionization is the main driving mechanism for the CLs. Moreover, Gelbord et al. (2009) used the sixth SDSS data release (Adelman-McCarthy et al. 2008) to analyze the CLR in 63 AGNs with [Fe X] λ6374 (IP = 233.60 eV), [Fe XI] λ7892 (IP = 262.10 eV), and [Fe VII] λ6086 (IP = 99.10 eV) emission. They used X-ray observations from Rosat (Voges et al. 1999, 2000) to similarly posit that AGN photoionization is the main ionization source of the CLs. Finally, Reefe et al. (2022) executed the first systematic survey of 20 optical CLs in the spectra of nearly 1 million galaxies from the eighth SDSS data release (Aihara et al. 2011). The authors found that CL emission is extremely rare (≈0.03% of the sample show at least one CL), and that the highest ionization potential CLs tend to be found in lower-mass galaxies. They reasoned that this finding is consistent with theory that hotter accretion disks are produced by lower-mass black holes, which typically reside in lower-mass galaxies.

Here, we use MaNGA's 11th, and final, data release (MPL-11; 10,010 unique galaxies) to further resolve the physics of the CLR, and to better understand the relationship between the production of CLs and AGN activity. With our custom pipeline, we identify 71 unique galaxies with emission from either [Ne V]λ3347, λ3427, [Fe VII]λ3586, λ3760, λ6086, or [Fe X]λ6374 detected at $\geqslant 5\sigma$ above the continuum, which makes it the most extensive such catalog of MaNGA CL galaxies to date.

This paper is outlined as follows: Section 2 details the technical components of the SDSS-IV MaNGA survey and its data pipeline, Section 3 describes the methodology we use to build the CL catalog and to analyze the physical properties of the CLR, Section 4 reviews our results, Section 5 provides interpretations of our findings, and Section 6 includes our conclusions and intended future work. All wavelengths are provided in vacuum, and we assume a Λ cold dark matter cosmology with the following values: $\Omega_M = 0.287$, $\Omega_\Lambda = 0.713$, and $H_0 = 69.3$ km s^{-1} Mpc^{-1}.

2. Observations

2.1. Sample of Galaxies

We assemble our sample from the SDSS-IV MaNGA catalog (Bundy et al. 2015; Drory et al. 2015; Law et al. 2016; Yan et al. 2016; Blanton et al. 2017; Wake et al. 2017). MaNGA observations occurred between 2014 and 2020, using the SDSS 2.5 m telescope (Gunn et al. 2006). The IFS survey contains data for 10,010 nearby galaxies ($0.01 < z < 0.15$; average $z \approx 0.03$) with stellar mass distributions between $10^9\ M_\odot$ and $10^{12}\ M_\odot$. The spectra were taken at wavelengths between 3622

and 10354 Å, with a typical spectral resolving power of ≈2000, corresponding to a velocity resolution of ≈60 km s^{-1} (see Bundy et al. 2015).

MaNGA contains spectroscopic maps out to at least 1.5 times the effective radius; the typical galaxy is mapped out to a radius of 15 kpc. Each MaNGA spatial pixel, or spaxel, covers $0\farcs5 \times 0\farcs5$, and the average FWHM of the on-sky point-spread function (PSF) is $2\farcs5$, which corresponds to a typical spatial resolution of 1–2 kpc (Drory et al. 2015).

2.2. MaNGA Data Analysis Pipeline

The MaNGA Data Analysis Pipeline (DAP; Westfall et al. 2019) offers publicly available high-level data products. The MaNGA DAP algorithms have been in development since 2014, and its main outputs are stellar kinematics, fluxes, and kinematics of prominent emission lines, and continuum spectral indices. To measure each parameter, the DAP relies on spectral fitting with pPXF (Cappellari 2012, 2017), where each fit features a blend of stellar templates with a multiplicative polynomial component to the stellar continuum. In particular, the DAP incorporates the MILESHC stellar templates library (Westfall et al. 2019) to fit the stellar kinematics.

The inputs for the DAP are data reduced by the MaNGA Data Reduction Pipeline (DRP). The DRP is fed spectra from the MaNGA fiber-feed system, which consists of 17 IFUs: two 19-fiber IFUs, four 37-fiber IFUs, four 61-fiber IFUs, two 91-fiber IFUs, and five 127-fiber IFUs (see Drory et al. 2015 for a more detailed description). The DRP subsequently wavelength, flux, and astrometrically calibrates the spectra.

3. Analysis

3.1. CL Continuum Subtraction and Emission-line Fitting

We scan for [Ne V]λ3347, λ3427, [Fe VII]λ3586, λ3760, λ6086, and [Fe X]λ6374 emission to better understand their effectiveness as AGN indicators. These CLs are selected because MaNGA's DAP does not provide emission-line measurements for them. As a result, we expand upon the custom pipeline detailed in Negus et al. (2021) to measure these CLs in MPL-11. Note that all 10 CL galaxies reported in Negus et al. (2021) are recovered using the new MPL-11 pipeline.

3.1.1. CL Stellar Continuum Subtraction

To measure the stellar kinematics, and subsequently subtract the stellar continuum for each CL galaxy's observed spectra, we use pPXF (Cappellari 2012, 2017). pPXF performs a polynomial fit on each galaxy's spectrum while masking gas emission lines. For each fit, we use the MILES[8] stellar templates library to represent the stellar population synthesis model. This library contains ≈1000 stars, with spectra obtained by the Isaac Newton Telescope. These spectra cover the wavelength range of 3525–7500 Å at a 2.5 Å FWHM resolution.

We first access the DRP to extract the necessary data cubes for each MaNGA galaxy before performing the pPXF stellar continuum subtraction. The data cubes provide a spectrum for each individual spaxel across the FOV of each galaxy. We then use the spectroscopic redshifts of each galaxy, adopted from the NASA Sloan Atlas catalogs (Blanton et al. 2011), to adjust the spectra to rest vacuum wavelengths. We also use a minimum redshift threshold (z_{min}) for CLs near the lower wavelength limit of MaNGA (3622 Å; Table 1) to ensure CLs of interest are not shifted out of MaNGA's spectral coverage. For [Ne V]λ3347, λ3427 and [Fe VII]λ3586, ≈93% (9152), ≈83% (8096), and ≈3% (229) of the MPL-11 galaxies, respectively, feature redshifts that place each CL out of MaNGA's spectral range; as a result, we are unable to scan for [Ne V]λ3347, λ3427 and [Fe VII]λ3586 in these respective galaxies.

Table 1
Target CLs

Emission Line	Wavelength (Å)	IP (eV)	z_{min}
[Ne V]	3347	97.1	0.088
[Ne V]	3427	97.1	0.061
[Fe VII]	3586	99.1	0.016
[Fe VII]	3760	99.1	…
[Fe VII]	6086	99.1	…
[Fe X]	6374	233.6	…

Note. Columns are (1) emission line, (2) rest wavelength, (3) ionization potential, and (4) minimum redshift value required for MaNGA detection.

We then apply a mask to each datacube, such that the imported wavelength range for each spectrum matches the wavelength range of the stellar templates library (3525–7500 Å). Next, we normalize each spectrum by dividing fluxes in this wavelength range by each spectrum's median flux value (to avoid numerical issues; see Cappellari 2017 for a more detailed discussion). Subsequently, we define a typical instrument resolution of ≈2.5 Å, construct a set of Gaussian emission-line templates (to mask emission lines; provided by pPXF), and fit the stellar templates. Note that for the CLs near the lower limit of the mask (3525 Å; e.g., [Ne V]λ3347, λ3427 and [Fe VII]λ3586), we perform a custom stellar continuum fit and subtraction before measuring the target emission line. In these instances, we execute a polynomial fit on a narrow spectral region, ≈300 Å wide, of continuum (free of prominent absorption or emission lines) near the rest wavelength of the target CL to model the background stellar continuum and subtract it from the spectrum.

3.1.2. [Ne V] and [Fe VII] Emission-line Measurements

Once the spectra are stellar continuum subtracted, we attempt a single Gaussian fit on a ≈30 Å region centered on the rest wavelengths of the CLs ([Fe X]λ6374 being the exception; see Section 3.1.3). We found that this wavelength range is adequate for capturing the full extent of CL emission in our preliminary scans. We then determine the rms flux of two continuum regions (≈60 Å wide) that neighbor each target CL, free of absorption or emission lines, and require that CL amplitudes are detected at $\geqslant 5\sigma$ above the mean rms flux values in these continuum regions. We consider the spectral resolution of MaNGA ($R = \lambda/\Delta\lambda \approx 1400$ at 3600 Å; $R \approx 2000$ at 6000 Å; Smee et al. 2013) to eliminate fits with $\Delta\lambda \lessapprox 2.4$ Å (for [Ne V]λ3347, λ3427), $\lessapprox 2.6$ Å (for [Fe VII]λ3586, λ3760), and $\lessapprox 3$ Å (for [Fe VII]λ6086 and [Fe X]λ6374). We provide an example of a single Gaussian fit for the [Fe VII]λ3586 line in Figure 1.

[8] http://miles.iac.es/

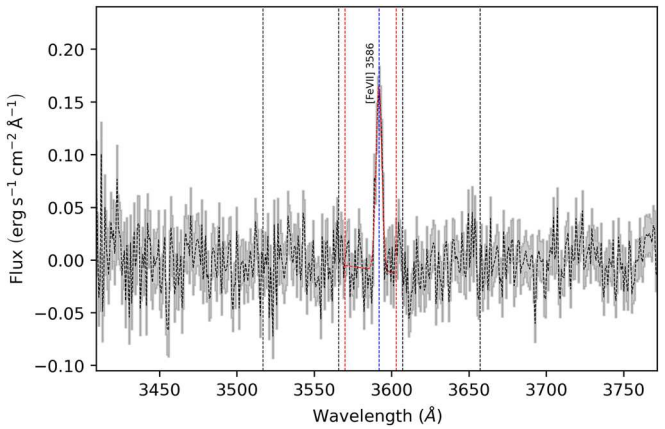

Figure 1. A sample spectrum from an individual spaxel showing the [Fe VII] λ3586 line detected at $\geqslant 5\sigma$ above the continuum in J0906. The dotted black line is the continuum subtracted spectrum, the shaded gray region is the uncertainty, the solid red line represents the best fit, the red dotted vertical lines mark the fitting window, the blue dotted line signifies the rest wavelength of the [Fe VII]λ3586 line, and the two sets of black dotted vertical lines correspond to the neighboring continuum windows where the rms flux values of the continuum are calculated.

3.1.3. [Fe X] Emission-line Measurements

For [Fe X]λ6374, the broad blue wing of this line is often blended with [O I]λ6364 due to their close proximity. Consequently, we attempt a double Gaussian fit to isolate the [Fe X]λ6374 line. If this routine does not successfully fit both lines with $\geqslant 5\sigma$ confidence, then we attempt a single Gaussian fit and apply the method used in Gelbord et al. (2009) and Rose et al. (2015), whereby the emission-line ratio [O I]λ6300/λ6364 is used to determine if the [O I]λ6364 and [Fe X]λ6374 lines are blended. Specifically, from atomic physics, if [O I] $\lambda 6300/\lambda 6364 = 3$, then the [O I]$\lambda$6364 line is free from contamination (see also Elmhamdi 2011 for a full review). If [Fe X]λ6374 emission is present and blended with [O I]λ6364, it will reduce the [O I]λ6300/λ6364 ratio below three. The MaNGA DAP provides flux values for both [O I]λ6364 and [O I]λ6300 lines. We adopt this method and require this ratio to be below three when fitting for [Fe X]λ6374 with a single Gaussian fit to avoid confusing [O I]λ6364 and [Fe X]λ6374 emission. Once we isolate the [Fe X]λ6374 emission, we impose the same thresholds used to identify the [Ne V] and [Fe VII] emission lines (e.g., amplitudes $\geqslant 5\sigma$; Section 3.1.2).

3.2. Coronal Line Flux Maps

Similar to Negus et al. (2021), we create custom CL flux maps to analyze the strength and distribution of the CLs in the CLR. We create these maps using the integrated CL flux value from each spaxel for each CL galaxy (Figure 2).

The center of each MaNGA observation corresponds to the galactic center (Yan et al. 2016). We use this position and the galaxy's inclination angle to determine the de-projected galactocentric distance of each CL spaxel. We do acknowledge that the CL gas may not be restricted to the galactic disk; i.e., the CL emission may associated with an ionization "cone" and therefore, in these instances, the de-projected distances are approximations.

The MaNGA DAP provides the ratio of the semiminor to semimajor axes (b/a) for each galaxy, and we use this value to determine the cosine of each galaxy's inclination angle (i): $\cos(i) = b/a$. The de-projected distance of each CL spaxel to the center of the galaxy is then measured by:

$$\mathrm{CLD} = \sqrt{(x - x_{\mathrm{center}})^2 + ((y - y_{\mathrm{center}}) * \cos(i))^2} \quad (1)$$

where x is the projected distance between the spaxel and the galaxy center measured along the galaxy's major axis, and y for the minor axis.

We then convert spaxel distances to a physical unit (kiloparsecs) using the `astropy.cosmology` Python package. The resulting value corresponds to the coronal line distance (CLD) of each CL-emitting spaxel from the galactic center. Further, the minimum coronal line distance ($\mathrm{CLD_{min}}$) corresponds to the distance of each galaxy's closest CL-emitting spaxel from the galactic center. Finally, the maximum coronal line distance ($\mathrm{CLD_{max}}$) corresponds to the distance of each galaxy's most distant CL-emitting spaxel from the galactic center.

3.3. Galaxy Morphology

To uncover the correlation, if any, between CL emission and galaxy morphology (e.g., spiral and elliptical), we use the MaNGA Morphologies Galaxy Zoo value-added catalog to classify the morphologies of the galaxies in our sample. This catalog features data from Galaxy Zoo 2, a "citizen science" catalog with more than 16 million visual morphological classifications for >304,000 galaxies in SDSS (GZ2; Willett et al. 2013),

The weighted vote fraction (discussed in Willett et al. 2013) accounts for voter consistency when participants select morphological classifications, and we require this fraction to be $\geqslant$50% before assigning a morphological classification (e.g., "E" for elliptical, or "S" for spiral). We also use the weighted vote fraction to determine if a CL galaxy features a bar, and/or is categorized as odd ("b" and "o," respectively).

In addition, to determine the fraction of CL galaxies undergoing a merger, we consider the analysis being performed by R. Nevin et al. (2023, in preparation) ("Nevin catalog" hereafter). The authors determine the merger probability for each of the 1.3 million galaxies in the SDSS DR16 photometric sample, using a statistical learning tool that is built on a linear discriminant analysis framework, which is trained to separate mock images of simulated merging and nonmerging galaxies using imaging predictors (see Nevin et al. 2019 for a full review). We investigate the MPL-11 galaxies from the broader SDSS DR16 Nevin catalog, and classify a CL galaxy as a merger if the Nevin catalog gives it a merger value (p_{merg}) > 0.5.

3.4. AGN Bolometric and [O III] Luminosities

The AGN bolometric luminosity effectively traces the energetic output of an AGN (across the entire electromagnetic spectrum). To compare the luminosity of the CL AGN candidates with other known AGN candidates, we thus consider the bolometric luminosity parameter.

We determine the AGN bolometric luminosity for each CL galaxy using the summed [O III] flux values ($F_{[\mathrm{O\ III}]}$) across the entire galaxy (provided by the MaNGA DAP), and the procedure outlined in Pennell et al. (2017), which assumes

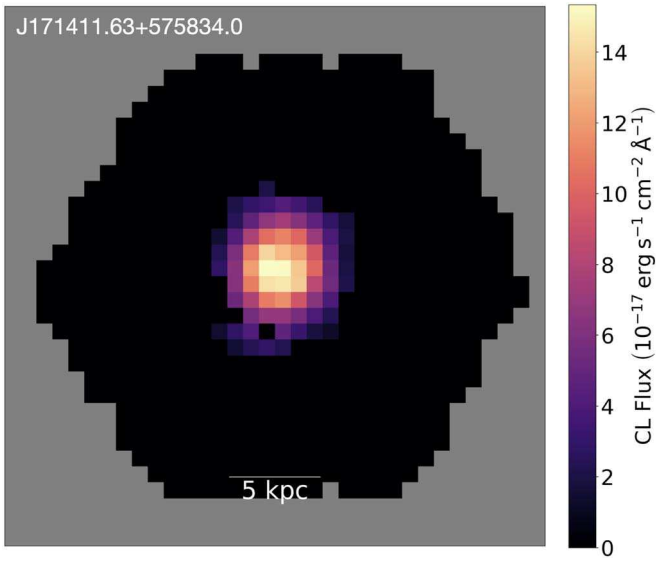

Figure 2. A sample CL flux map showing [Ne V]λ3427 emission detected $\geqslant 5\sigma$ above the continuum in J1714. For this galaxy, the strongest [Ne V]λ3427 emission is located near the center of the galaxy. The gray region is outside of the MaNGA FOV, and the black region comprises spaxels with no CL emission. North is up, south is down, east is to the left, and west is to the right.

[O III] emission comes from an AGN:

$$\log\left(\frac{L_{\rm bol}}{\rm erg\ s^{-1}}\right) = (0.5617 \pm 0.0978)\log\left(\frac{L_{\rm [O\ III]}}{\rm erg\ s^{-1}}\right) + (21.186 \pm 4.164) \quad (2)$$

where $L_{\rm [O\ III]}{=}F_{\rm [O\ III]}(4\pi R^2)$, and R is the DAP provided luminosity distance based on redshift and a standard cosmology of $\Omega_M = 0.3$ and $\Omega_\Lambda = 0.7$ (redshift is also measured by the DAP).

We then measure the total [O III] luminosity (using the summed [O III] fluxes across the entire galaxy) for each CL galaxy in our sample. Next, we compare the [O III] luminosities of the CLs in our pipeline (Section 4.3) to determine the relative strength of [O III] for each CL. We do so to assess if specific CLs are preferentially found in higher or lower-luminosity [O III]-emitting galaxies, which is useful to determine if CLs uniformly trace all AGNs, or if there may be an [O III] luminosity dependence.

3.5. Narrow-line BPT Diagnostics Diagrams

Baldwin–Phillips–Terlevich optical emission-line diagnostic diagrams (BPT diagrams; Baldwin et al. 1981; Veilleux & Osterbrock 1987; Kewley et al. 2001, 2006) are widely accepted to be effective tools for categorizing gas ionization sources as star-forming, Seyfert (AGN), low-ionization nuclear emission-line region, or a composite of multiple ionization sources. They serve as the traditional AGN selection tool for most spectroscopic surveys. Specifically, these diagrams compare line ratios between high and low-ionization species, most commonly [O III]λ5007/Hβ versus [N II]λ6583/Hα ("[N II]/Hα diagram" hereafter).

In this paper, we construct spatially resolved narrow-line BPT diagnostic diagrams for the CL galaxies to better constrain the ionization sources of the CLs. To do so, we require emission-line measurements for the [N II]λ6583, [O III]λ5007, Hα, and Hβ emission lines. The DAP measures the continuum subtracted flux for each of these emission lines. Note that these fluxes account for galactic reddening using the $E(B-V)$ values determined by the DRP, which assumes an O'Donnell (1994) reddening law.

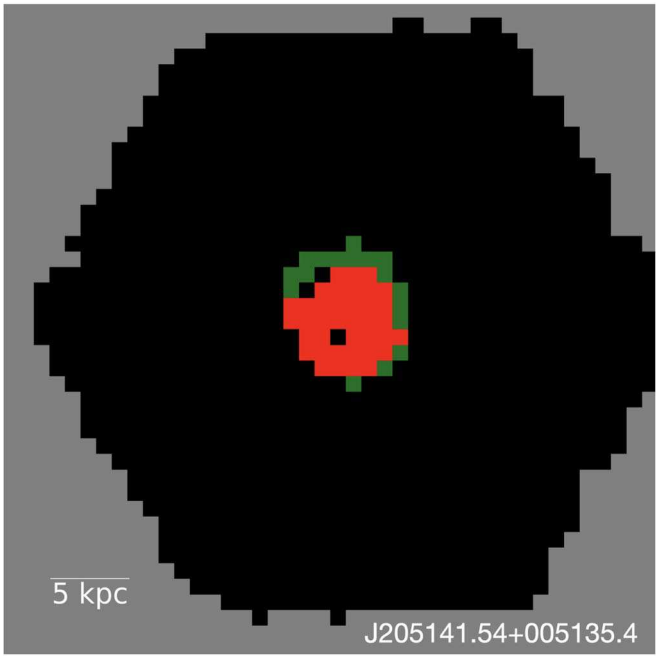

Figure 3. A sample BPT map showing AGN spaxels in red and composite spaxels in green, for CL-emitting spaxels in J2051 (a [Ne V]λ3427 galaxy). The gray region is outside of the MaNGA FOV, and the black region comprises spaxels with no CL emission. North is up, south is down, east is to the left, and west is to the right.

Once we determine the necessary emission-line flux measurements, we compute the ratios for the [N II]/Hα diagram, for each CL-emitting spaxel. We then use these values to create custom spatially resolved BPT maps, whereby we present the BPT classification for each CL-emitting spaxel within the MaNGA FOV, for each CL galaxy. Figure 3 shows an example BPT map.

3.6. Dust Attenuation

Mullaney et al. (2009) investigated the [Fe VII]λ6086, [Fe X]λ6374, and [Fe XI]λ7892 emission lines in the Seyfert 1 galaxy Ark 564. The authors used the photoionization code CLOUDY (Ferland et al. 1998) to determine the location and kinematics of these lines. They found that the CLs are launched from a dusty torus near the SMBH, where the gas is quickly accelerated. Moreover, using the CLOUDY models, they determined that some iron carrying grains are destroyed during the initial acceleration of the gas.

To follow up on the analysis performed by Mullaney et al. (2009), and to better understand the role of dust grains on the potential depletion of the iron CLs, we use the $E(B-V)$ color excess index. This index traces the degree of interstellar reddening caused by photons that are scattered off of dust; in essence, it measures the difference between an object's observed color index and its intrinsic color index. $E(B-V)$ values for each CL galaxy are provided by the MaNGA DRP (using Schlegel et al. 1998 maps), and assume the extinction law provided by O'Donnell (1994).

3.7. Shock Diagnostics

We explore the role of shocks (e.g., supernova remnant, SNR, and [O I]λ6300 ("[O I]" hereafter) shocks) in our analysis to elucidate the role of collisional excitation in the production CLs (e.g., Penston et al. 1984). To do so, we consider the strength of the [S II]λ6717, λ6731 doublet with respect to the Hα line, which has traditionally been used to differentiate SNR shocks from photoionized regions. Specifically, Dodorico (1978) and Dodorico et al. (1980) first determined that regions with [S II] $(\lambda6717 + \lambda6731)/\mathrm{H}\alpha > 0.4$ can be used to identify SNR shocks. Additionally, the [O I] emission line is generally a strong tracer of shock excitation, and line flux ratios with [O I]/H$\alpha > 0.1$ indicate that shocks with velocities 160–300 km s^{-1} are the main excitation source of [O I] (e.g., Dopita 1976; Allen et al. 2008; Farage et al. 2010; Rich et al. 2010, 2011; Riffel et al. 2021; Comerford et al. 2022). The MaNGA DAP provides flux measurements for the [S II]λ6717, λ6731, [O I], and Hα emission lines.

4. Results

In this section, we report the main findings for the CL galaxies in our sample. First, we present the fraction of confirmed AGNs in the CL galaxies. Then, we analyze the spatial distribution and extent of the CLs. Next, we inspect the CL galaxy bolometric and [O III] luminosities to deduce the effectiveness of using each species for accurate AGN identification. After, we assess the BPT classification of the CL-emitting spaxels. Finally, we investigate the role of dust extinction and shocks in the CLR to determine the impact of dust grains on CL emission, and to further constrain the ionization source(s) of the CLs.

In total, we find 71 galaxies with CL emission at $\geqslant 5\sigma$ above the background continuum in MaNGA's MPL-11 (33 feature [Ne V] emission, 39 feature [Fe VII] emission, and four feature [Fe X] emission). Note that, in our sample, 40 unique CL galaxies with either [Ne V]λ3427, [Fe VII], or [Fe X] emission, or a combination of the three, feature redshifts below the z_{min} threshold for [Ne V]λ3347 ($z_{\mathrm{min}} = 0.088$); furthermore, 24 unique CL galaxies with either [Fe VII] or [Fe X] emission feature redshifts below the z_{min} threshold for [Ne V]λ3427 ($z_{\mathrm{min}} = 0.061$). Therefore, we are unable to scan for [Ne V] λ3347 or [Ne V]λ3427 in these respective galaxies. In general, most of the MPL-11 galaxies feature redshifts that place [Ne V] λ3347, λ3427 out of MaNGA's spectral range (see Section 3.1.1).

Moreover, in light of the extensive work to detect AGNs using infrared CLs, we crossmatched our catalog of 71 unique CL galaxies with the infrared CL catalogs presented in Genzel et al. (1998), Sturm et al. (2002), Armus et al. (2004, 2022), Lutz et al. (2005), Weedman et al. (2006), Dasyra et al. (2008), and Goulding & Alexander (2009). We do not identify any of the MaNGA CL galaxies in these samples.

For 63/71 CL galaxies with GZ2 classifications (89%), we determine a nearly even fraction of spirals and ellipticals (48% and 52%, respectively). In addition, we measure the average size of the CLR (from the galactic center) for [Ne V]λ3347, λ3427, [Fe VII]λ3586, λ3760, λ6086, and [Fe X]λ6374 to be 1.9 kpc, 2.3 kpc, 3.7 kpc, 5.3 kpc, 4.1 kpc, and 2.5 kpc, respectively (Table 2). Further, we find that the vast majority of [Ne V] galaxies feature at least one CL-emitting spaxel in their nuclear regions (98.5%; $2\farcs5 \times 2\farcs5$ FOV surrounding the central spaxel), whereas [Fe VII] and [Fe X] galaxies generally feature a smaller fraction (73% and 75%, respectively). The corresponding fractions of confirmed AGNs in these galaxies (determined by comparing our sample to the largest catalog of confirmed MaNGA AGNs; Section 4.1) are 94%, 14%, and 25%, respectively.

4.1. MaNGA AGN Comparison

Comerford et al. (2023, in preparation) provide the most complete sample of AGN in MaNGA's MPL-11 (see Comerford et al. 2020 for a full review of their MPL-8 MaNGA AGN catalog). The authors compile a catalog of MaNGA AGNs that were detected using SDSS broad emission lines, NRAO Very Large Array Sky Survey (NVSS)/Faint Images of the Radio Sky at Twenty Centimeters (FIRST) 1.4 GHz radio observations, Wide-field Infrared Survey Explorer (WISE) mid-infrared color cuts, and Swift/BAT hard X-ray observations.

Broad Balmer emission lines (FWHM > 1000 km s^{-1}) are strong tracers of the rapidly rotating, high density gas, near the SMBH. They serve as reliable tracers for AGN activity. Oh et al. (2015) assembled a catalog of nearby ($z \leqslant 2$) Type I AGNs in SDSS's seventh data release using the broad Hα emission line, and Comerford et al. (2023, in preparation) identified 78 broad-line AGNs from this catalog in MPL-11.

Powerful AGN radio jets can expand several kiloparsecs from the SMBH, and can thus serve as strong signatures for AGN activity. As a result, detecting the radio emission from these sources is a great tool for accurate AGN identification. Best & Heckman (2012) used observations from the 1.4 GHz NVSS (Condon et al. 1998) and FIRST (Becker et al. 1995) to detect AGNs in the SDSS's seventh data release (DR7). They differentiated AGN activity from star formation emission using the correlation between the 4000 Å break strength and radio luminosity per stellar mass, emission-line diagnostics, and the relation between Hα and radio luminosity (Becker et al. 1995). Comerford et al. (2023, in preparation) found 221 radio AGNs from this catalog in MPL-11.

Heated dust that surrounds an AGN can produce mid-infrared emission, which can expose obscured and unobscured AGN activity. Comerford et al. (2023, in preparation) thus relied upon observations from WISE (Wright et al. 2010) to help identify AGNs. They consider the four bands observed with WISE (3.4 μm (W1), 4.6 μm (W2), 12 μm (W3), and 22 μm (W4)) and apply a 75% reliability criteria of $\mathrm{W1} - \mathrm{W2} > 0.486\ \exp\{0.092(\mathrm{W2}-13.07)^2\}$ and $\mathrm{W2} > 13.07$, or $\mathrm{W1} - \mathrm{W2} > 0.486$ and $\mathrm{W2} \leqslant 13.07$ (Assef et al. 2018) to select AGNs. J. Comerford et al. (2023, in preparation) detected 130 WISE AGNs in MPL-11.

X-ray emission produced by AGNs generally results from inverse Compton scattering of low-energy UV photons by energetic electrons from the accretion disk (e.g., Haardt & Maraschi 1991; Antonucci 1993; Hinkle & Mushotzky 2021). Therefore, X-rays can be a useful indicator of AGN activity. Accordingly, the authors use the X-ray catalog assembled by Oh et al. (2018), which consists of ≈1000 AGNs observed by the Swift Observatory's Burst Alert Telescope (BAT) in the ultra-hard X-ray (14–195 keV), to detect AGNs. J. Comerford et al. (2023, in preparation) uncovered 30 AGNs from this catalog in MPL-11.

We compare our CL sample to the AGN catalog reported by J. Comerford et al. (2023, in preparation; "Comerford sample"

Table 2
Spatial Properties for the CL Galaxies

Detected CL (1)	Wavelength (Å) (2)	Confirmed Galaxies (3)	Nuclear Emission (%) (4)	CLD_{min} (kpc) (5)	CLD_{max} (kpc) (6)	CLD_{avg} (kpc) (7)
[Ne V]	3347	8	100	0.52	5.3	1.9
[Ne V]	3427	33	97	0.34	19	2.3
[Fe VII]	3586	4	100	0.10	9.6	3.7
[Fe VII]	3760	16	56	0.11	36	5.3
[Fe VII]	6086	19	63	0.10	21	4.1
[Fe X]	6374	4	75	0.60	4.9	2.5

Note. Columns are: (1) detected CL, (2) rest wavelength, (3) number of galaxies with CL emission detected, (4) percentage of CL galaxies with at least one CL-emitting spaxel in a nuclear 2.″5 FOV, (5) the average CLD (distance of CL-emitting spaxel from the galaxy center), (6) the distance of the farthest CL-emitting spaxel from the galaxy center, and (7) the distance of the closest CL-emitting spaxel from the galaxy center.

hereafter) and crossmatch 35 CL galaxies in it (52% of our sample). Further, we consider the fraction of CL galaxies with confirmed AGNs by specific CL species. We determine that 94% (31/33) of the [Ne V] galaxies host an AGN; 14% (5/36) of the [Fe VII] galaxies and 25% (1/4) of the [Fe X] galaxies. Overall, 35 unique CL galaxies host a confirmed AGN; 80% (28/35) are confirmed with WISE observations, 63% (22/35) with broad Balmer emission lines, 14% (5/35) with NVSS observations, and 11% (4/35) with BAT AGNs.

All of the [Ne V]λ3347 galaxies feature an AGN and [Ne V] λ3427 emission, and of the five [Fe VII] galaxies with a confirmed AGN, two (J0736 and J1714) also feature both [Ne V]λ3347, λ3427 emission. Further, two of the remaining three [Fe VII] galaxies with a confirmed AGN (J0807 and J1157) feature emission from more than one [Fe VII] emission line (J0807 features [Fe VII]λ3586, λ3760, λ6086 emission; J1157 features [Fe VII]λ3586, λ3760 emission). The final [Fe VII] galaxy with a confirmed AGN exclusively features [Fe VII]λ6086 emission, and the sole [Fe X] galaxy with a confirmed AGN (J1628) exclusively features [Fe X] emission.

Provided that 80% of the CL galaxies in our sample are confirmed to host an AGN via WISE diagnostics, we consider the fact that these WISE diagnostics are likely to miss low-luminosity AGNs (e.g., Assef et al. 2018). Perhaps, one possible explanation for the discrepancy in AGNs across the CLs in our sample is that [Ne V] traces high-luminosity AGNs, while [Fe VII] and [Fe X] may possibly trace low-luminosity AGNs. We explore this further in Sections 4.3 and 4.5.

4.2. Spatial Distribution and Extent of the CLs

To better constrain the ionization source(s) of the CLs, we first map the measured fluxes of the CLs within the MaNGA FOV for each CL galaxy (Figure 2). These flux maps provide a snapshot of the orientation, extent, and intensity of CL emission for the galaxies in our sample. Then, we compute the de-projected distance of each CL spaxel from the nuclear center of each galaxy (i.e., the photometric center; Section 3.2) to determine the distance of each CL-emitting spaxel from the galaxy center. Finally, we define the nuclear region of each CL galaxy to be a $2.''5 \times 2.''5$ aperture (5×5 spaxel grid; where each spaxel covers a $0.''5 \times 0.''5$ FOV) surrounding the central spaxel.

If AGN photoionization is the primary mechanism producing the CLs, it is likely that CL emission is predominantly within the nuclear region of each galaxy, close to the SMBH and the accretion disk (e.g., Gelbord et al. 2009; Mazzalay et al. 2010). On the other hand, if shocks, AGN outflows, or stellar processes play an active role in generating CLs, we anticipate that CL emission will not be found exclusively in the nuclear region. Rather, we would expect to find emission in regions off-center or off-axis from the SMBH and the galaxy's rotational plane (see Negus et al. 2021 for more discussion).

To analyze the CL distribution within the nuclear region of the CL galaxies, we measure the fraction of CL galaxies with at least one CL-emitting spaxel in their center, for each CL (Table 2). We find that the vast majority of [Ne V] λ3347, λ3427 galaxies feature at least one [Ne V]-emitting spaxel in their nuclear regions (100% and 97%, respectively). This finding is consistent with our results in Section 4.1, that [Ne V] is a strong tracer of AGN activity (i.e., CL emission is likely dominated by AGN photoionization near the SMBH). Comparatively, the fraction of CL galaxies with nuclear emission from [Fe VII] λ3586, λ3760, or λ6086 varies significantly more (100%, 56%, and 63%, respectively).

In Figure 4, we present a sample of CL flux maps for six representative CL galaxies. In three of the galaxies (J1104, J1349, and J2152), it is apparent that the source of the CLs is within the nuclear region, as the CL flux is concentrated here. However, for the three remaining galaxies (J0023, J1613, and J0920), the CL-emitting spaxels are highly offset from the nuclear region. Based on the orientation of the CL flux in J0023 and J0920, it is possible that AGN outflows are generating the CL since the CL emission is generally perpendicular to the orbital plane of each galaxy. For the J1613 observation, we determine that several optical emission lines (e.g., [O III] and Hα) measured in the secondary galaxy (with the featured "CL emission;" southwest of J1613 in the MaNGA FOV) have large velocity shifts ($>$2000 km s^{-1}) compared to the center of J1613, which suggests this may not be a companion galaxy (i.e., this is not a merging system; J1613 is not in the Nevin catalog). As a result, the "CL emission" in this galaxy is likely from a separate emission line, from a background galaxy with a different redshift than the primary galaxy. For J1349, we acknowledge that there appears to be a visual companion galaxy near the nuclear region; it is possible that both merger-induced shocks and AGN photoionization could be producing the CL emission. In addition, we suspect that dust grains may also have a significant impact on the presence of [Fe VII] and [Fe X] emission in our sample. In Section 4.5, we review the likelihood of iron depletion by dust grains more thoroughly.

We also compute the CLDs for the CL galaxies. The CLD, which is the distance of each CL-emitting spaxel from the galactic center, reveals the physical scale of the CLR for each

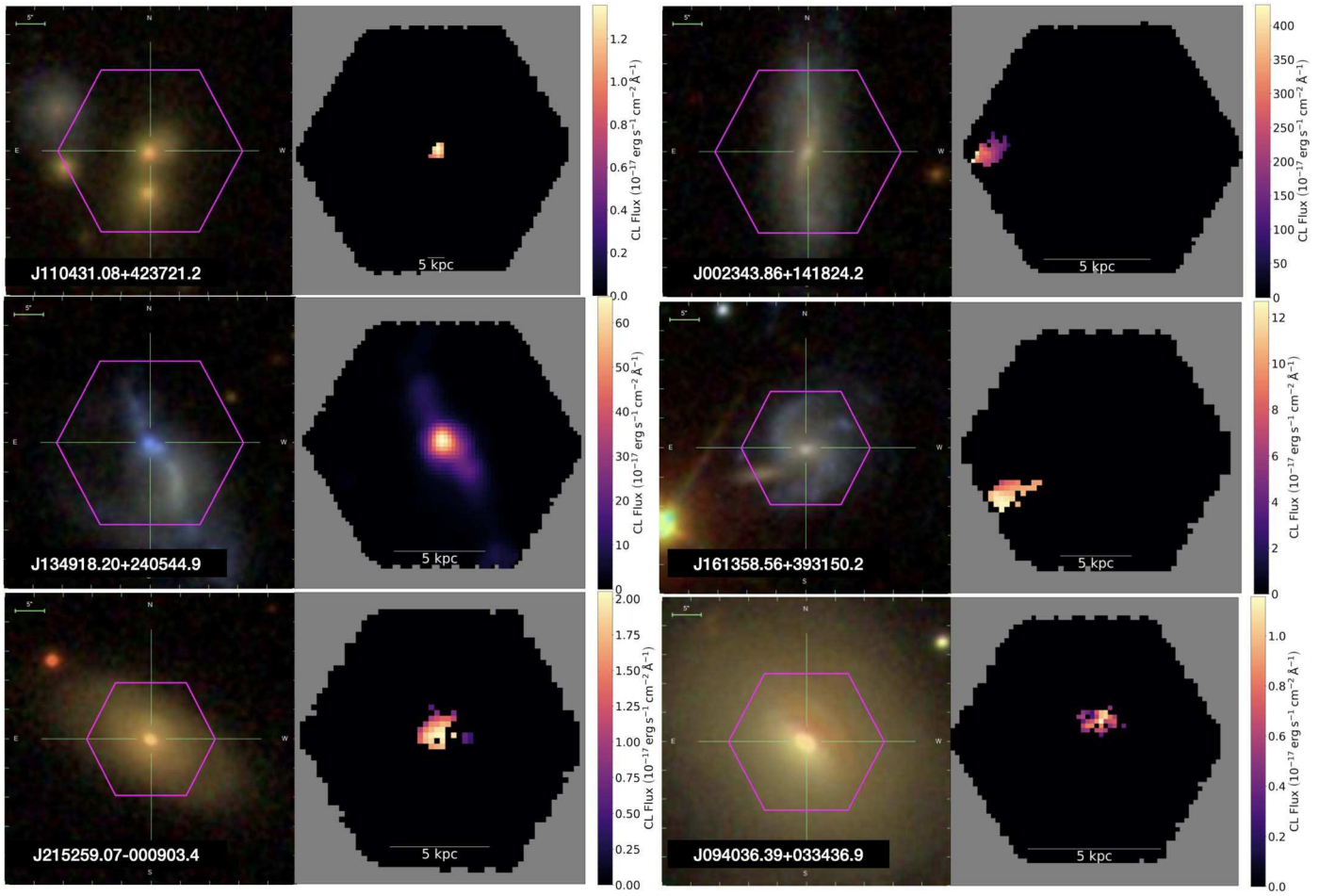

Figure 4. CL flux maps for 6/71 CL galaxies in our sample. From top to bottom and left to right: J1104 ([Ne V]λ3427 map), J0023 ([Fe VII]λ3760 map), J1349 ([Fe VII]λ3760 map), J1613 ([Fe VII]λ3760 map), J2152 ([Fe VII]λ6086 map), and J0940 ([Fe VII]λ6086 map). For J0023 and J0940, the maps display CL emission spatially offset from the galaxy center. For each galaxy, the emission is offset perpendicular to the rotational plane of the galaxy, suggestive of the source of the CLs being AGN outflows. For J1349 we observe a possible companion galaxy and consider the possibility that these two galaxies are undergoing a merger. For the J1613 observation, we determine that several optical emission lines (e.g., [O III] and Hα) measured in the secondary galaxy (with the featured "CL emission;" southwest of J1613 in the MaNGA FOV) have large velocity shifts (>2000 km s^{-1}) compared to the center of J1613, which suggests this may not be a companion galaxy (i.e., this is not a merging system; J1613 is not in the Nevin catalog). As a result, the "CL emission" in this galaxy is likely from a separate emission line, from a background galaxy with a different redshift than the primary galaxy. For J1104 and J2152, CL emission is concentrated toward the galaxy center, likely produced by AGN photoionization.

CL galaxy. We measure the average CLDs for [Ne V]λ3347, λ3427 to be 1.9 kpc and 2.3 kpc, respectively; 3.7 kpc, 5.3 kpc, and 4.1 kpc for [Fe VII]λ3586, λ3760, λ6086, respectively; and 2.5 kpc for [Fe X]λ6374. We find no correlation between IPs and CLDs (IP = 262.1 eV for [Fe X], IP = 126.2 eV for [Ne V], and IP = 125 eV for [Fe VII]). Moreover, for the [Ne V] galaxies, the minimum and maximum distances of each CL-emitting spaxel from the nuclear center (labeled CLD_{min} and CLD_{max} in Table 2) ranges between 340 pc and 19 kpc, 100 pc and 36 kpc for the [Fe VII] galaxies, and 600 pc and 4.9 kpc for the [Fe X] galaxies. These large variances in CL distance suggest that the CLR extends from just beyond the BLR (≈0.1 kpc) and well into the NLR (several kiloparsecs).

Finally, to confirm that CL emission is indeed resolved for each CL galaxy, we consider the instrument PSF (≈2.″5 for MaNGA), and find that 60/71 CL galaxies show resolved and continuous emission in excess of the typical instrument PSF. The remaining 11 CL galaxies (J0205, J1010, J1117, J1317, J1344, J1416, J1604, J1626, J1628, J1658, and J1649) lack CL emission in excess of the typical instrument PSF. We reason that these CLRs are below the instrument PSF, and not spatially resolved. As discussed in Negus et al. (2021), these CLRs may still be spatially resolved by other instruments (e.g., Mazzalay et al. 2010 and their use of STIS/HST optical spectra), and it is also possible that CL emission may be oriented along an ionization cone; however, here we consider the CLDs of these galaxies to be upper limits.

4.3. AGN Bolometric and [O III] Luminosities

AGN bolometric luminosity, which scales with [O III] luminosity, is effectively the "power" of an AGN. As outlined in Pennell et al. (2017), [O III] emission is the most utilized line for measuring bolometric luminosity, due its strength in most AGN spectra and the relatively weak blending of emission from photoionized gas in star-forming regions with the line (e.g., Heckman et al. 2004; Heckman & Best 2014).

Therefore, to help resolve the discrepancy between the differing fractions of confirmed AGNs in our sample (Section 4.1; 94% of the [Ne V] galaxies feature a confirmed AGN, 14% for the [Fe VII] galaxies, and 25% of the [Fe X] galaxies; for CL galaxies with multiple CLs, we measure this

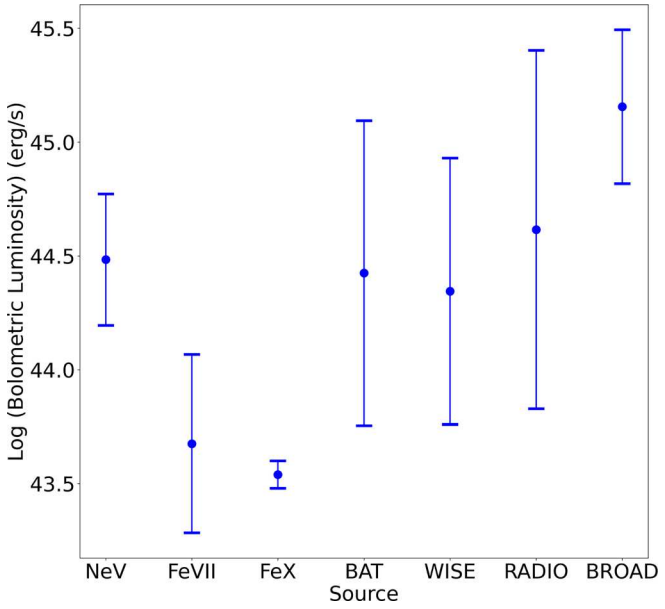

Figure 5. Average mean bolometric luminosities for the 71 CL galaxies in our sample (analyzed by each CL species; [Ne V], [Fe VII], and [Fe X]), compared to the MaNGA galaxies confirmed to feature an AGN in the Comerford sample. The AGNs in the Comerford sample were verified using SDSS broad emission lines, NVSS/FIRST 1.4 GHz radio observations, WISE mid-infrared color cuts, and Swift/BAT hard X-ray observations. The mean bolometric luminosity of the [Ne V] galaxies, $\log(L_{\rm bol}) = 44.5$ erg s^{-1}, is consistent with the AGNs reported in the Comerford sample (mean $\log(L_{\rm bol}) = 44.6$ erg s^{-1} for the Comerford sample). However, the [Fe VII] and [Fe X] galaxies feature mean bolometric luminosities an order of magnitude lower ($\log(L_{\rm bol}) \leqslant 43.7$ erg s^{-1}) than the Comerford sample. We suspect that the [Fe VII] and [Fe X] emission lines may primarily be detecting low-luminosity AGNs in MaNGA.

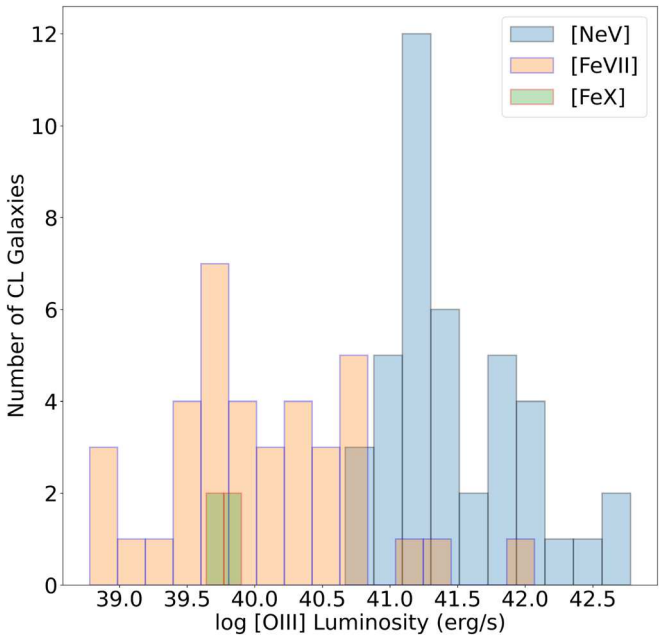

Figure 6. The log([O III]) luminosity distribution for the 71 CL galaxies. The blue, orange, and green histograms represent the [Ne V], [Fe VII], and [Fe X] galaxies in our sample, respectively. [Ne V] emitting galaxies tend to have higher [O III] luminosities than [Fe VII] or [Fe X], which suggests that these galaxies may host higher-luminosity AGNs. The means of the [Ne V] log ([O III]) luminosity distribution are 41.5 erg s^{-1}, and 40.1 erg s^{-1} and 39.8 erg s^{-1} for [Fe VII] and [Fe X], respectively.

fraction independently for each CL), and to evaluate the overall effectiveness of using CL detections to identify AGNs, we consider the bolometric and [O III] luminosities of the CL galaxies, and further inspect the Comerford sample of MaNGA AGN. In particular, we compare the mean bolometric luminosities of the CL galaxies ($L_{\rm bol}$; using the summed [O III] flux across the entire galaxy; Section 3.4) with the total population of MPL-11 AGN in the Comerford sample (Section 4.1; Figure 5).

We find that the mean bolometric luminosity for the [Ne V] galaxies (mean $z = 0.10$; median $z = 0.11$), $\log(L_{\rm bol}) = 44.5$ erg s^{-1}, is consistent with the mean value of Comerford's population of MaNGA galaxies that host an AGN ($\log(L_{\rm bol}) = 44.6$ erg s^{-1}). On the other hand, we measure the mean bolometric luminosities of the [Fe VII] galaxies (mean $z = 0.06$; median $z = 0.05$) and the [Fe X] galaxies (mean $z = 0.07$; median $z = 0.06$) to be an order of magnitude lower than the mean $\log(L_{\rm bol})$ value of the Comerford sample ($\log(L_{\rm bol}) = 43.7$ erg s^{-1} and $\log(L_{\rm bol}) = 43.5$ erg s^{-1} for the [Fe VII] and [Fe X] galaxies, respectively). Note that we also present the [O III] luminosity distribution for the CL galaxies in Figure 6 (the mean [O III] luminosities for the [Ne V] galaxies are 41.5 erg s^{-1}, and 40.1 erg s^{-1} and 39.8 erg s^{-1} for the [Fe VII] and [Fe X] galaxies, respectively). We reason that the [Fe VII] and [Fe X] galaxies may be preferentially tracing lower-luminosity AGN in MaNGA, which are generally more difficult to detect in multiwavelength observations.

However, we find that the five [Fe VII] galaxies with a confirmed AGN (J0736, J0807, J1157, J1535, and J1714) all feature relatively high [O III] luminosities of $\log(L_{\rm [O\ III]}) \gtrapprox 41$ erg s^{-1}. Additionally, the three remaining [Fe VII] galaxies with [O III] luminosities at or above this limit (without confirmed AGNs) are J0906, J1349, and J2152. Both J0906 and J1349 visually appear to be actively undergoing a merger; J2152 shows no apparent companion galaxy. We reason that, for the [Fe VII] galaxies in our sample, the $\log(L_{\rm [O\ III]})$ cutoff of $\approx$41 erg s^{-1} is a useful threshold for identifying confirmed AGNs (from the Comerford sample) and may also be helpful for detecting mergers. Further, for the [Ne V] galaxies, J1344 features the lowest [O III] luminosity ($\log(L_{\rm [O\ III]}) = 40.6$ erg s^{-1}) and in fact hosts a confirmed AGN. We consider the [O III] luminosity threshold for the [Fe VII] galaxies ($\log(L_{\rm [O\ III]}) \approx 41$ erg s^{-1}) to be similar for the [Ne V] galaxies.

We also determine that the two [Ne V] galaxies (J1658 and J1104) that do not feature a confirmed AGN (out of 33 total [Ne V] galaxies), feature [O III] luminosities of $\log(L_{\rm [O\ III]}) = 41.2$ erg s^{-1} and $\log(L_{\rm [O\ III]}) = 41.4$ erg s^{-1}, respectively. Considering these high [O III] luminosities, and the high [Ne V] AGN detection rate (94%), we propose that these two galaxies are strong AGN candidates.

On the other hand, the one [Fe X] galaxy with a confirmed AGN, J1628, features an [O III] luminosity of $\log(L_{\rm [O\ III]}) = 39.8$ erg s^{-1} (the remaining three [Fe X] galaxies, which do not host a confirmed AGN, also have log([O III]) luminosities $<$40 erg s^{-1}). Consequently, while we consider the $\log(L_{\rm [O\ III]}) \approx 41$ erg s^{-1} threshold useful for identifying CL galaxies with a confirmed AGN, it is important to acknowledge that CL galaxies with a confirmed AGN can have [O III] luminosities below this limit.

4.4. BPT Analysis

The BPT diagram has long served as the standard tool for identifying ionization mechanisms in emission-line sources (e.g., Baldwin et al. 1981; Veilleux & Osterbrock 1987;

Table 3
BPT Classifications for the CL Galaxies

Detected CL	Rest Wavelength (Å)	Confirmed CL Galaxies	Confirmed AGN	Confirmed AGN Fraction (%)	[N II] AGN Fraction (%)	[N II] Composite Fraction (%)	[N II] SF Fraction (%)
(1)	(2)	(3)	(4)	(5)	(6)	(7)	(8)
[Ne V]	λ3347	8	8	100	87.5	12.5	0
	λ3427	33	31	94	90	10	0
[Fe VII]	λ3586	4	3	75	78.5	19	2.5
	λ3760	16	2	13	80.3	5.8	13.9
	λ6086	19	3	16	67.9	19.7	12.5
[Fe X]	λ6374	4	1	25	88.3	0	11.7

Note. Columns are: (1) detected CL, (2) rest wavelength, (3) the number of galaxies that feature emission from the respective line, (4) the fraction of galaxies that host a confirmed AGN, (5) the average fraction of [N II] AGN BPT spaxels, (6) the average fraction of [N II] Composite BPT spaxels, and (7) the average fraction of [N II] SF BPT spaxels.

Kewley et al. 2001, 2006). While effects such as stellar shocks and emission from post-AGB stars are liable to elevate star-forming (SF) sources beyond the AGN threshold (see Yan & Blanton 2012; Belfiore et al. 2016; Agostino & Salim 2019 for a further discussion), we nonetheless explore the BPT classification for each CL-emitting spaxel to help pin down the source of CL emission in our sample. To do so, we compute the $\log([\mathrm{O\,III}]/\mathrm{H}\beta)$ and $\log([\mathrm{N\,II}]/\mathrm{H}\alpha)$ ratios required for the $[\mathrm{N\,II}]/\mathrm{H}\alpha$ diagram (Section 3.5). Using the thresholds outlined in Kewley et al. (2006), we categorize each CL spaxel as either [H II] (i.e., star-forming), AGN, or a composite of the two. Note that for some CL-spaxels, the DAP reports negative values for the necessary emission-line fluxes, likely because the emission lines of interest yield low flux levels and the DAP's subtraction of the stellar continuum results in a net absorption at the expected wavelength of the emission line. As such, we exclude these spaxels from our analysis.

For the [Ne V], [Fe VII], and [Fe X] emission lines, we determine that, on average, the majority of CL-emitting spaxels are AGNs or composite (Table 3). For [Ne V]λ3347, λ3427, we find that 87.5% and 90% of these spaxels are classified as AGNs, respectively; 12.5% and 10% as composite, respectively; and 0% as SF for both. Moreover, we measure the BPT ratios for the [Fe VII]λ3586, λ3760, λ6086 spaxels, and find that 78.5%, 80.3%, and 67.9% of these spaxels are classified as AGNs, respectively; 19%, 5.8%, and 19.7% as composite, respectively; and 2.5%, 13.9%, and 12.5% as SF, respectively. For [Fe X]λ6374, 88.3% of the CL-emitting spaxels are classified as AGNs; 0% as composite; and 11.7% as SF. In total, 100% of the [Ne V] spaxels in our sample are either BPT AGNs or BPT composite, 91% of the [Fe VII] spaxels, and 88.3% of the [Fe X] spaxels. These results suggest that the CLs are perhaps useful tracers of AGNs, and that the lack of confirmed AGNs in our [Fe VII] and [Fe X] galaxies may trace back to the nearly bimodal log([O III]) and bolometric luminosity distributions presented in Section 4.3 (i.e., [Fe VII] and [Fe X] may generally be found in low-luminosity AGNs that are potentially missed by traditional AGN detection techniques; although, it is also possible that [Fe VII] and [Fe X] may not host an AGN at all). We explore this possibility, and the corresponding impact of dust extinction on iron CL emission in Section 4.5.

Table 4
CLR Dust Attenuation

Detected CL	Wavelength (Å)	Average $E(B-V)$ Value
(1)	(2)	(3)
[Ne V]	3347	0.057
	3427	0.045
[Fe VII]	3586	0.045
	3760	0.029
	6086	0.039
[Fe X]	6374	0.049

Note. Columns are (1) detected CL, (2) rest wavelength, and (3) average $E(B-V)$ values, for each CL, reported by MaNGA's DRP.

4.5. The Impact of Dust on CL Emission

The role of dust extinction (i.e., the impact of dust grains) on CL emission has yet to be fully unraveled. Mullaney et al. (2009) suggested that dust grains can potentially deplete heavier CL species (e.g., iron). Further, Ferguson et al. (1997) posited that there are three primary effects of dust on line formation: (1) emission lines weaken due to the absorption of the incident continuum by dust, (2) grains photoelectrially heat the gas, and (3) some of the gas-phase elements (e.g., iron) are depleted (see also Seab & Shull 1983; Snow & Witt 1996; Collins et al. 2009; Kraemer et al. 2009). Comparatively, Ferguson et al. (1997) contended that neon (a noble gas; i.e., a species of gas with a full outer shell of valence electrons, and thus less chemical reactivity) is significantly less depleted by dust grains, and therefore [Ne V] is emitted almost fully outside the grain sublimation radii. Here, we consider the likelihood that a significant population of iron CL photons are destroyed by dust in our sample.

To explore the role of dust extinction on CL emission in our sample, and to determine its relevance for the discrepancy between the fraction of confirmed AGNs in the [Ne V] galaxies (94%) versus the [Fe VII] and [Fe X] galaxies (14% and 25% respectively; Section 4.1), we use the $E(B-V)$ color excess index, which traces interstellar reddening (Section 3.6). The MaNGA DRP provides this index for each galaxy in MPL-11, and we use it to determine if there is a correlation between the dust content of each CL galaxy and its CL emission. We present our findings in Table 4.

In particular, we find the mean $E(B-V)$ values for the [Fe VII]λ3760, λ6086 galaxies to be the lowest (i.e., feature less dust grains) across our sample (0.029 and 0.039, respectively). Because iron is susceptible to destruction by dust grains, particularly in the nuclear region where the presence of dust is greater (also due to dust in the NLR), these relatively low values provide a viable explanation for the presence of [Fe VII]λ3760, λ6086 emission in these galaxies; for reference, our sample contains 16 [Fe VII]λ3760 galaxies and 19 [Fe VII]λ6086 galaxies. Comparatively, the [Ne V] λ3347, λ3427, [Fe VII]λ3586, and [Fe X]λ6374 galaxies feature higher mean $E(B-V)$ values; 0.057, 0.045, 0.045, and 0.049, respectively. The corresponding number of iron CL-emitting galaxies found in these galaxies is only nine in total (J0736 features emission from both [Ne V] lines, as well as [Fe VII]λ3586 emission; J1714 features emission from both [Ne V] lines, as well as [Fe VII]λ6086 emission; J0807 features emission from [Fe VII]λ3586, λ3760, λ6086; J1157 features emission from [Fe VII]λ3586, λ3760; J0906 features emission from [Fe VII]λ3586; and J1628, J2311, J1649, and J1720 exclusively feature emission from [Fe X]λ6374). We suspect that emission from the iron CL species is being diminished within these relatively dusty galaxies, which provides a physical explanation for the low number of iron CL galaxies in the high $E(B-V)$ value galaxies $E(B-V)\geqslant 0.045$; nine iron CL galaxies) versus the low $E(B-V)$ galaxies ($E(B-V)<0.039$; 34 iron CL galaxies).

Furthermore, Elitzur & Shlosman (2006) considered the correlation between the AGN dusty torus and AGN bolometric luminosity. They proposed that the dusty torus diminishes at $\log(L_{\rm bol})\lessapprox 42$ erg s^{-1}, due to mass accretion no longer being able to sustain the necessary cloud outflow rate, which effectively results in a decrease in column density (see also Chiaberge et al. 1999; Whysong & Antonucci 2004; Maoz et al. 2005). While the cloud component of the AGN is not immediately extinguished below this threshold, the authors contend that the cloud outflow rate at $\log(L_{\rm bol})\lessapprox 42$ erg s^{-1} is less than the necessary "standard" observed in higher-luminosity AGNs. As a result, we consider the $L_{\rm bol}$ values for the CL species (Figure 5, mean $\log(L_{\rm bol})\geqslant 44.3$ erg s^{-1} for [Ne V] galaxies; mean $\log(L_{\rm bol})\leqslant 43.7$ erg s^{-1} for the [Fe VII] and [Fe X] galaxies) to conclude that the lower $L_{\rm bol}$ values correlate with a diminishing dusty torus, which results in less destruction of iron by dust grains. Accordingly, we detect more iron CLs in these low-luminosity sources. On the other hand, the [Ne V] galaxies feature higher $L_{\rm bol}$ values, which likely correspond to their elevated $E(B-V)$ values. Likewise, since $L_{\rm bol}$ scales with $L_{\rm O\,III}$, this reasoning elucidates the nearly bimodal $\log(L_{\rm O\,III})$ distribution of the [Ne V] versus the [Fe VII] and [Fe X] galaxies (Figure 6; the mean of the [Ne V] log ([O III]) luminosity distribution is 41.5 erg s^{-1}, and 40.1 erg s^{-1} and 39.8 erg s^{-1} for [Fe VII] and [Fe X], respectively).

4.6. SNR, [O I], and Merger-induced Shocks in the CLR

Astrophysical shocks can result from a variety of mechanisms, which include, but are not limited to, galaxy collisions, SNRs, cloud-cloud collisions, expanding H II regions, and outflows from young stellar objects (see Allen et al. 2008 for a further review). To deduce the role of shocks in the CLR, we consider the [S II] $(\lambda6717+\lambda6731)/{\rm H}\alpha$ and [O I]$\lambda6300/{\rm H}\alpha$ ratios for each CL-emitting spaxel in our sample (values >0.4 indicate SNR shocks and values >0.1 trace [O I] shocks, respectively; Section 3.7).

We also investigate the fraction of CL galaxies actively undergoing a merger using the Nevin et al., catalog (Table 5; Table 6; Section 3.3). In Negus et al. (2021), we found that the 3/10 CL galaxies without a confirmed AGN were all strong merger candidates (J0906, J1349, and J1454). Therefore, we consider the possibility that companion galaxies can drive gas inflows toward the galactic centers, resulting in merger-induced shock excitation (e.g., Farage et al. 2010) that may also produce CLs. Using the Nevin catalog, here we determine that 32/66 of the CL galaxies (48%; five CL galaxies are not reported in the Nevin catalog: J0752, J0920, J1306, J1613, and J2132) have $p_{\rm merg}$ values >0.5—indicative of an ongoing merger.

Further, we present our SNR and [O I] shocks results in Tables 7 and 8. Overall, we find that the fraction of SNR and [O I] shocks do not vary significantly for the CL galaxies. In particular, on average and across all CL species, 42% of the CL-emitting spaxels in the CL galaxies with a confirmed AGN feature SNR shocks (35% feature [O I] shocks), whereas 56% of the CL-emitting spaxels in the CL galaxies without a confirmed AGN feature SNR shocks (49% feature [O I] shocks). Further, on average and across all CL species, 32% of the CL-emitting spaxels in the CL galaxies undergoing a merger feature SNR shocks (38% feature [O I] shocks). On the other hand, 36% of the CL-emitting spaxels in the CL galaxies not undergoing a merger feature SNR shocks (27% feature [O I] shocks). Finally, on average and across all CL species, 41% of the CL-emitting spaxels in the CL galaxies with nuclear CL emission feature SNR shocks (32% feature [O I] shocks). Comparatively, 27% of the CL-emitting spaxels in the CL galaxies without nuclear CL emission feature SNR shocks (44% feature [O I] shocks).

We find clear evidence of SNRs and [O I] shocks in the CL-emitting spaxels of each CL species in our sample. However, the fraction of these shocks does not strongly trace CL galaxies with or without: a confirmed AGN, a companion galaxy, or nuclear CL emission. We reason that SNRs and [O I] shocks may be viable CL-emission mechanisms; however, they are not likely dominant, and we find little evidence that they produce CLs away from the nuclear region, in the absence of a confirmed AGN, or when a merging companion galaxy is present.

5. Discussion

Based on our findings, we reason that the efficacy of using CLs to detect AGNs varies by species of CL. While the ionization potential of each CL is $\geqslant$100 eV (Table 1; well above the 55 eV threshold for pure star formation; consistent with the strong continuum of an AGN being the ionization source), we find that certain CLs are better at identifying higher-luminosity AGNs than others ($\log(L_{\rm [O\,III]})\gtrapprox 41$ erg s^{-1}). In particular, [Ne V] emission is predominately present in higher [O III] luminosity galaxies that feature a confirmed AGN (mean $\log(L_{\rm [O\,III]})=41.5$ erg s^{-1} for the [Ne V] galaxies; 94% of the [Ne V] galaxies host a confirmed AGN). On the other hand, we detect [Fe VII] and [Fe X] emission in lower [O III] luminosity galaxies with fewer confirmed AGNs (mean $\log(L_{\rm [O\,III]})\leqslant 40.1$ erg s^{-1} for both CLs; 14% and 25% confirmed AGNs for the [Fe VII] and [Fe X] galaxies, respectively).

Table 5
Morphological and Merger Classifications of the CL Galaxies

SDSS Name (1)	Detected CL(s) (2)	Redshift (3)	Morphology (4)	Merger (5)
J001938.78+144201.1	[Fe VII]λ6086	0.116	E	N
J002343.86+141824.2	[Fe VII]λ3760	0.018	S(b)	N
J020557.03+004623.9	[Fe VII]λ6086	0.042	E	N
J021257.59+140610.2	[Ne V]λ3427	0.062	⋯	N
J030639.57+000343.1	[Ne V]λ3427	0.107	E	Y
J072656.07+410136.0	[Ne V]λ3427	0.129	S(b)	Y
J073623.13+392617.7	[Ne V]λ3347, [Ne V]λ3427, [Fe VII]λ3586	0.118	⋯	Y
J074128.48+442431.6	[Ne V]λ3427	0.132	E	N
J075217.84+193542.2	[Ne V]λ3427	0.117	⋯	⋯
J075756.71+395936.1	[Ne V]λ3427	0.066	E(o)	Y
J080018.53+461112.3	[Fe VII]λ3760	0.061	E	N
J080403.40+404809.3	[Ne V]λ3427	0.126	S	Y
J080543.32+252710.9	[Fe VII]λ3760	0.072	E	Y
J080707.18+361400.5	[Fe VII]λ3586, [Fe VII]λ3760, [Fe VII]λ6086	0.032	S	N
J080859.19+364112.9	[Fe VII]λ6086	0.03	E	Y
J084002.36+294902.6	[Ne V]λ3427	0.065	E	N
J085208.48+511845.8	[Fe VII]λ3760	0.115	S	N
J085601.94+572327.4	[Fe VII]λ6086	0.041	S(bo)	N
J085835.98+013149.5	[Ne V]λ3427	0.107	S(b)	Y
J090659.46+204810.0	[Fe VII]λ3586	0.109	S(o)	N
J092002.85+054407.7	[Fe VII]λ6086	0.038	S(b)	⋯
J092739.77+050312.5	[Ne V]λ3427	0.126	S	N
J094036.39+033436.9	[Fe VII]λ6086	0.016	⋯	Y
J101042.59+061157.0	[Ne V]λ3427	0.098	E(o)	Y
J103825.16-002331.1	[Ne V]λ3347, [Ne V]λ3427	0.096	S(o)	Y
J105439.31+475144.2	[Ne V]λ3427	0.073	S(b)	N
J105759.31+404940.6	[Fe VII]λ6086	0.024	E	Y
J110431.08+423721.2	[Ne V]λ3427	0.126	E(o)	Y
J111403.52+472653.4	[Fe VII]λ3760	0.113	E	Y
J111711.79+465134.0	[Fe VII]λ3760	0.061	E	N
J111724.94+443347.8	[Fe VII]λ3760	0.066	E	N
J111803.22+450646.8	[Ne V]λ3347, [Ne V]λ3427	0.107	E(o)	Y
J112043.79+534337.4	[Fe VII]λ6086	0.107	E	N
J115710.68+221746.2	[Fe VII]λ3586, [Fe VII]λ3760	0.052	S(b)	N
J122443.43+442438.8	[Ne V]λ3427	0.126	E	Y
J123521.03+422002.6	[Fe VII]λ6086	0.039	E	N
J130626.65+451720.4	[Fe VII]λ6086	0.051	E	⋯
J131730.11+474659.3	[Fe VII]λ3760	0.027	E	N
J134401.90+255628.3	[Ne V]λ3427	0.062	S(b)	N
J134918.20+240544.9	[Fe VII]λ3760	0.021	⋯	Y
J141623.14+381127.4	[Ne V]λ3427	0.135	⋯	Y
J142004.29+470716.8	[Ne V]λ3427	0.07	S(b)	N
J144454.24+522648.5	[Fe VII]λ3760	0.146	E	N

Note. Columns are: (1) SDSS name, (2) detected CL(s), (3) redshift, (4) GZ2 morphological classifications; "E" is for elliptical, "S" is for spiral, "b" is for bar, "o" is for odd, and "⋯" indicates no morphological classification was assigned, and (5) the merger classification from the Nevin catalog; "Y" marks galaxies with $p_{\rm merg} > 0.5$, "N" identifies galaxies with $p_{\rm merg} \leqslant 0.5$, and "⋯" represents galaxies that are not in the Nevin catalog.

We reason that the destruction of iron CLs by dust grains, which we find is inversely proportional to AGN bolometric luminosity (the dusty torus diminishes at $\log(L_{\rm bol}) \lessapprox 42$ erg s^{-1}; e.g., Elitzur & Shlosman 2006), may be directly impacting [Fe VII] and [Fe X] emission; the CL galaxies with the lowest $E(B-V)$ values yield the most iron CL detections (nine iron CL galaxies with $E(B-V) \geqslant 0.045$; 34 iron CL galaxies with ($E(B-V) < 0.039$). We posit that if the [Fe VII] and [Fe X] galaxies host AGNs, that they may be lower-luminosity AGNs, which are potentially too weak to be detected via SDSS broad emission lines, NVSS/FIRST 1.4 GHz radio observations, WISE mid-infrared color cuts, and Swift/BAT hard X-ray observations.

We determine that there are primarily two distinct populations of CL galaxies in our sample: (1) a subset of CL galaxies that emit [Ne V] (33/71 CL galaxies), with relatively high [O III] and bolometric luminosities, and a high fraction of confirmed AGNs (94%), and (2) a group of CL galaxies that emit [Fe VII] and [Fe X] (40/71 CL galaxies), with relatively low [O III] and bolometric luminosities, and a low fraction of confirmed AGNs (14% and 25%, respectively).

Overall, we consider the similar IPs of [Ne V] and [Fe VII] (126.2 eV and 125 eV, respectively), the high IP of [Fe X] (262.21 eV), and our BPT analysis (100% of the [Ne V] spaxels in our sample are either BPT AGNs or NPT composite, 91% of the [Fe VII] spaxels, and 88.3% of the [Fe X] spaxels; Table 3),

Table 6
Morphological and Merger Classifications of the CL Galaxies (Continued)

SDSS Name (1)	CL (2)	Redshift (3)	Morphology (4)	Merger (5)
J145420.10+470022.3	[Fe VII]λ3760	0.126	E(o)	Y
J151600.58+342119.1	[Ne V]λ3427	0.125	S(o)	Y
J151856.39+332152.2	[Fe VII]λ6086	0.069	E	N
J153552.40+575409.4	[Fe VII]λ6086	0.03	E(o)	N
J160455.20+280956.9	[Ne V]λ3427	0.077	S	Y
J161301.62+371714.9	[Ne V]λ3427	0.069	S(b)	Y
J161358.56+393150.2	[Fe VII]λ3760	0.038	S	⋯
J161413.20+260416.3	[Ne V]λ3347, [Ne V]λ3427	0.131	⋯(o)	Y
J162428.39+483548.0	[Fe VII]λ6086	0.057	E(o)	Y
J162621.91+405442.7	[Fe VII]λ3760	0.03	S(o)	Y
J162845.89+252938.0	[Fe X]λ6374	0.04	E	N
J162908.95+383256.6	[Fe VII]λ6086	0.033	E	N
J163014.63+261223.3	[Ne V]λ3347, [Ne V]λ3427	0.131	S(b)	N
J163053.84+243343.5	[Fe VII]λ6086	0.063	E	Y
J163430.87+374143.6	[Ne V]λ3427	0.099	E	N
J164956.39+351243.5	[Fe X]λ6374	0.1	E	N
J165810.10+622456.3	[Ne V]λ3427	0.119	S(b)	N
J171411.63+575834.0	[Ne V]λ3347, [Ne V]λ3427, [Fe VII]λ6086	0.093	E	Y
J172032.02+280602.9	[Fe X]λ6374	0.083	⋯	Y
J205141.54+005135.4	[Ne V]λ3347, [Ne V]λ3427	0.106	S	Y
J211646.34+110237.4	[Ne V]λ3427	0.081	S	Y
J212401.89-002158.6	[Ne V]λ3427	0.062	S(b)	Y
J212900.75+001057.3	[Fe VII]λ3760	0.133	E(o)	N
J213227.90+100816.9	[Ne V]λ3427	0.063	S(o)	⋯
J215259.07-000903.4	[Fe VII]λ6086	0.028	S	N
J223338.41+131243.6	[Ne V]λ3347, [Ne V]λ3427	0.093	S	Y
J231142.05+150638.2	[Fe X]λ6374	0.04	S(o)	N
J232538.54+152115.8	[Fe VII]λ6086	0.041	S	N

Note. Columns are: (1) SDSS name, (2) detected CL(s), (3) redshift, (4) GZ2 morphological classifications; "E" is for elliptical, "S" is for spiral, "b" is for bar, "o" is for odd, and "⋯" indicates no morphological classification was assigned, and (5) the merger classification from the Nevin catalog; "Y" marks galaxies with $p_{\rm merg} > 0.5$, "N" identifies galaxies with $p_{\rm merg} \leqslant 0.5$, and "⋯" represents galaxies that are not in the Nevin catalog.

Table 7
SNR Shocks

Detected CL (1)	Wavelength (Å) (2)	CL AGN SNR Shocks (3)	CL Non-AGN SNR Shocks (4)	CL Mergers SNR Shocks (5)	CL Nonmergers SNR Shocks (6)	CL Nuclear SNR Shocks (7)	CL Nonnuclear SNR Shocks (8)
[Ne V]	3347	13%	⋯	14%	0%	13%	⋯
[Ne V]	3427	33%	100%	30%	50%	39%	0%
[Fe VII]	3586	3%	38%	0%	8%	12%	⋯
[Fe VII]	3760	6%	55%	49%	49%	52%	45%
[Fe VII]	6086	95%	42%	64%	41%	61%	25%
[Fe X]	6374	100%	45%	36%	67%	67%	36%

Note. Columns are: (1) detected CL, (2) rest wavelength, (3) percentage of CL-emitting spaxels in the CL galaxies with a confirmed AGN that feature SNR shocks, (4) percentage of CL-emitting spaxels in the CL galaxies without a confirmed AGN that feature SNR shocks, (5) percentage of CL-emitting spaxels in the CL galaxies undergoing a merger that feature SNR shocks, (6) percentage of CL-emitting spaxels in the CL galaxies not undergoing a merger that feature SNR shocks, (7) percentage of CL-emitting spaxels in the CL galaxies with nuclear CL emission (see Section 4.2) that feature SNR shocks, and (8) percentage of CL-emitting spaxels in the CL galaxies without nuclear CL emission that feature SNR shocks. "⋯" indicates an empty sample set.

to deduce that each CL in our sample is likely linked to AGN activity, but that [Fe VII] and [Fe X] emission may preferentially be found in less-luminous AGNs (we also consider the possibility that some of the iron CL emission may not exclusively be produced by AGNs; e.g., shocks may also play a role). We conclude that the BPT diagram is generally effective at tracing large populations of AGNs; however, [Ne V], in particular, can also be used as an additional resource to help trace AGNs, specifically for instances where one or more of the optical BPT line ratios is unable to be determined.

Moreover, Ferguson et al. (1997) reported CL critical densities between 10^7 and 10^{10} cm^{-3}, which suggest that the CLR is a region between the classical NLR and the BLR. The authors also indicate that lower ionization CLs (e.g., [Ne V] and [Fe VII]; IPs $\approx$ 125 eV) are more likely to form in lower-density gas that should be spatially resolved. In contrast, higher

Table 8
[O I] Shocks

Detected CL (1)	Wavelength (Å) (2)	CL AGN SNR Shocks (3)	CL Non-AGN [O I] Shocks (4)	CL Mergers [O I] Shocks (5)	CL Nonmergers [O I] Shocks (6)	CL Nuclear [O I] Shocks (7)	CL Nonnuclear [O I] Shocks
[Ne V]	3347	25%	⋯	29%	0%	25%	⋯
[Ne V]	3427	29%	100%	33%	31%	35%	0%
[Fe VII]	3586	4%	12%	0%	6%	6%	⋯
[Fe VII]	3760	3%	28%	20%	26%	25%	25%
[Fe VII]	6086	50%	36%	45%	33%	31%	49%
[Fe X]	6374	100%	67%	100%	67%	67%	100%

Note. Columns are: (1) detected CL, (2) rest wavelength, (3) percentage of CL-emitting spaxels in the CL galaxies with a confirmed AGN that feature [O I] shocks, (4) percentage of CL-emitting spaxels in the CL galaxies without a confirmed AGN that feature [O I] shocks, (5) percentage of CL-emitting spaxels in the CL galaxies undergoing a merger that feature [O I] shocks, (6) percentage of CL-emitting spaxels in the CL galaxies not undergoing a merger that feature [O I] shocks, (7) percentage of CL-emitting spaxels in the CL galaxies with nuclear CL emission (see Section 4.2) that feature [O I] shocks, and (8) percentage of CL-emitting spaxels in the CL galaxies without nuclear CL emission that feature [O I] shocks. "⋯" indicates an empty sample set.

ionization CLs (e.g., [Fe X]; IP = 262.1 eV) form in a region closer to the nucleus where the ionizing flux, and ionization parameters, are higher (i.e., these CLs form in denser, more efficiently emitting regions). Here we determine that the average sizes of the CLRs for [Ne V]λ3347, λ3427, [Fe VII] λ3586, λ3760, λ6086, and [Fe X]λ6374 are 1.9 kpc, 2.3 kpc, 3.7 kpc, 5.3 kpc, 4.1 kpc, and 2.5 kpc, respectively (Table 2)—well into the NLR for all CL species. With the enhanced capabilities of IFS, which enables us to spatially resolve the CLR, we find that the CLR for the galaxies in MaNGA is larger than reported in previous works (tens to hundreds of parsecs; e.g., Almudena Prieto et al. 2005; Mazzalay et al. 2010; Müller-Sánchez et al. 2011; Rodríguez-Ardila et al. 2011).

Finally, while the bulk of the CL galaxies in our sample feature CL emission in their nuclear regions (within a central $2\farcs5 \times 2\farcs5$ FOV; Section 4.2; Table 2), a significant fraction do not, which is inconsistent with pure AGN photoionization. In Section 4.6, we show that [O I] and SNR shocks are present in the CL-emitting spaxels of each CL species. However, the fraction of SNRs and [O I] shocks, across all CL species, do not significantly vary for the CL galaxies with or without nuclear CL emission. We reason, instead, that AGN radio jets or outflows may be interacting with gas clouds away from the nuclear region, ionizing them, and producing the noncentric CL emission we uncover in our sample (Figure 4; e.g., Tadhunter et al. 1988; Müller-Sánchez et al. 2011). It is also possible that this CL emission is tracing a different species of gas, that is not a CL, from a noncompanion galaxy within the MaNGA FOV (at a different redshift than the target galaxy; e.g., J1613—Figure 4).

6. Summary and Future Work

We construct the most extensive sample of MaNGA CL galaxies to date. With our custom pipeline, we measure emission from [Ne V]λ3347, [Ne V]λ3427, [Fe VII]λ3586, [Fe VII]λ3760, [Fe VII]λ6086, and/or [Fe X]λ6374 at $\geqslant 5\sigma$ above the background continuum in 71 galaxies in MaNGA's MPL-11 catalog of 10,010 unique galaxies.

Our main findings are:

1. The average size of the CLR for [Ne V], [Fe VII], and [Fe X] is 1.9 kpc, 3.8 kpc, and 2.5 kpc, respectively—beyond the BLR and into the traditional NLR.
2. The fractions of [Ne V], [Fe VII], and [Fe X] galaxies with at least one CL-emitting spaxel in their nuclear $2\farcs5$ region are 98.5%, 73%, and 75%, respectively. Nuclear CL emission is preferentially found in [Ne V] galaxies.
3. We identify two main populations of CL galaxies: (1) galaxies that mostly feature [Ne V] emission (33/71 CL galaxies), with relatively high [O III] and bolometric luminosities (mean [Ne V] log([O III]) luminosity = 41.5 erg s^{-1}, mean [Ne V] log($L_{\rm bol}$) = 44.5 erg s^{-1}), and a high fraction of confirmed AGNs (94%); and (2) galaxies that predominately emit [Fe VII] and [Fe X] (40/71 CL galaxies), with relatively low [O III] and bolometric luminosities (mean [Fe VII] and [Fe X] log([O III]) luminosities are 40.1 erg s^{-1} and 39.8 erg s^{-1}, respectively; mean [Fe VII] and [Fe X] log($L_{\rm bol}$) values are 43.7 erg s^{-1} and 43.5 erg s^{-1}, respectively), and a low fraction of confirmed AGNs (14% and 25%, respectively).
4. One-hundred percent of the [Ne V] spaxels in our sample are either BPT AGNs or BPT composite, 91% of the [Fe VII] spaxels, and 88.3% of the [Fe X] spaxels. The CLs are strong tracers of BPT AGN and BPT composite sources.
5. We detect a low number of iron CL galaxies in high $E(B-V)$ value galaxies ($E(B-V) \geqslant 0.045$; nine iron CL galaxies) versus low $E(B-V)$ galaxies ($E(B-V) < 0.039$; 34 iron CL galaxies). We reason that the destruction of iron CLs by dust grains, which is inversely proportional to AGN bolometric luminosity, may likely be depleting [Fe VII] and [Fe X] emission, particularly in the nuclear region where the presence of dust is greater. The [Fe VII] and [Fe X] galaxies may be tracing lower-luminosity AGNs, which are possibly too weak to be confirmed by traditional AGN detection techniques.
6. SNR and [O I] shock excitation are viable CL production mechanisms; however, they are not likely primary, as the abundance of SNRs and [O I] shocks does not vary significantly across our sample for galaxies with or without nuclear CL emission, an AGN, or a merging companion.

We will explore the CLR kinematics in a future publication to better comprehend the role of outflows on CL production. In particular, we will use [O III] flux maps to evaluate the

likelihood that AGN outflows produce CL emission, provided the strong correlation between [O III] emission and AGN outflows (e.g., Sun et al. 2017; Comerford et al. 2018). Further, we will measure the rotation and cloud velocities of the gas for each CL galaxy (to determine how the bulk motion of gas in the CL galaxies correlates with CL emission), and also analyze the emission-line profiles of the CLs to determine if, for example, the CLs feature any blueshifted emission—indicative of outflows.

Moreover, additional multiwavelength observations of the CLs would help deduce their nature. X-ray observations from Chandra, for example, would allow us to better confirm the population of low-luminosity AGNs in the CL galaxies. This will help to determine the effectiveness of using CL emission as an unambiguous tracer of AGNs in large-scale spectroscopic surveys of galaxies. Finally, our work here is also relevant for motivating near-IR measurements of additional CLs that are observable by the James Webb Space Telescope, particularly in cases where optical CLs may be obscured.

J.N. and J.M.C. acknowledge support from NSF AST 1714503 and NSF AST1847938.

Funding for the Sloan Digital Sky Survey IV has been provided by the Alfred P. Sloan Foundation, the U.S. Department of Energy Office of Science, and the Participating Institutions. SDSS-IV acknowledges support and resources from the Center for High-Performance Computing at the University of Utah. The SDSS website is www.sdss.org.

SDSS-IV is managed by the Astrophysical Research Consortium for the Participating Institutions of the SDSS Collaboration including the Brazilian Participation Group, the Carnegie Institution for Science, Carnegie Mellon University, the Chilean Participation Group, the French Participation Group, Harvard Smithsonian Center for Astrophysics, Instituto de Astrofísica de Canarias, The Johns Hopkins University, Kavli Institute for the Physics and Mathematics of the Universe (IPMU)/University of Tokyo, the Korean Participation Group, Lawrence Berkeley National Laboratory, Leibniz Institut für Astrophysik Potsdam (AIP), Max-Planck-Institut für Astronomie (MPIA Heidelberg), Max-Planck-Institut für Astrophysik (MPA Garching), Max-Planck-Institut für Extraterrestrische Physik (MPE), National Astronomical Observatories of China, New Mexico State University, New York University, University of Notre Dame, Observatário Nacional/MCTI, The Ohio State University, Pennsylvania State University, Shanghai Astronomical Observatory, United Kingdom Participation Group, Universidad Nacional Autónoma de México, University of Arizona, University of Colorado Boulder, University of Oxford, University of Portsmouth, University of Utah, University of Virginia, University of Washington, University of Wisconsin, Vanderbilt University, and Yale University.

This publication makes use of data products from the Wide-field Infrared Survey Explorer, which is a joint project of the University of California, Los Angeles, and the Jet Propulsion Laboratory/California Institute of Technology, funded by the National Aeronautics and Space Administration.

This research has made use of data supplied by the UK Swift Science Data Centre at the University of Leicester.

This work utilized the Summit supercomputer, which is supported by the National Science Foundation (awards ACI-1532235 and ACI-1532236), the University of Colorado Boulder, and Colorado State University. The Summit supercomputer is a joint effort of the University of Colorado Boulder and Colorado State University.

Software: This work made use of Astropy[9]: a community-developed core Python package and an ecosystem of tools and resources for astronomy (Astropy Collaboration et al. 2013, 2018, 2022).

ORCID iDs

James Negus https://orcid.org/0000-0003-2667-7645
Julia M. Comerford https://orcid.org/0000-0001-8627-4907
Francisco Müller Sánchez https://orcid.org/0000-0002-2713-0628
Mitchell Revalski https://orcid.org/0000-0002-4917-7873
Rogemar A. Riffel https://orcid.org/0000-0003-0483-3723
Kevin Bundy https://orcid.org/0000-0001-9742-3138
Rebecca Nevin https://orcid.org/0000-0003-1056-8401
Sandro B. Rembold https://orcid.org/0000-0003-0880-5738

References

Adelman-McCarthy, J. K., Agüeros, M. A., Allam, S. S., et al. 2008, ApJS, 175, 297
Agostino, C. J., & Salim, S. 2019, ApJ, 876, 12
Aihara, H., Allende Prieto, C., An, D., et al. 2011, ApJS, 193, 29
Allen, M. G., Groves, B. A., Dopita, M. A., et al. 2008, ApJS, 178, 20
Almudena Prieto, M., Marco, O., & Gallimore, J. 2005, MNRAS, 364, L28
Antonucci, R. 1993, ARA&A, 31, 473
Armus, L., Charmandaris, V., Spoon, H. W. W., et al. 2004, ApJS, 154, 178
Armus, L., Lai, T., & U, V. 2023, ApJL, 942, L37
Assef, R. J., Stern, D., Noirot, G., et al. 2018, ApJS, 234, 23
Astropy Collaboration, Price-Whelan, A. M., & Lim, P. L. 2022, ApJ, 935, 167
Astropy Collaboration, Price-Whelan, A. M., Sipőcz, B. M., et al. 2018, AJ, 156, 123
Astropy Collaboration, Robitaille, T. P., Tollerud, E. J., et al. 2013, A&A, 558, A33
Baldwin, J. A., Phillips, M. M., & Terlevich, R. 1981, PASP, 93, 5
Becker, R. H., White, R. L., & Helfand, D. J. 1995, ApJ, 450, 559
Belfiore, F., Maiolino, R., Maraston, C., et al. 2016, MNRAS, 461, 3111
Best, P. N., & Heckman, T. M. 2012, MNRAS, 421, 1569
Blanton, M. R., Bershady, M. A., Abolfathi, B., et al. 2017, AJ, 154, 28
Blanton, M. R., Kazin, E., Muna, D., et al. 2011, AJ, 142, 31
Bundy, K., Bershady, M. A., Law, D. R., et al. 2015, ApJ, 798, 7
Cappellari, M. 2012, pPXF: Penalized Pixel-Fitting Stellar Kinematics Extraction Astrophysics Source Code Library, ascl:1210.002
Cappellari, M. 2017, MNRAS, 466, 798
Chiaberge, M., Capetti, A., & Celotti, A. 1999, A&A, 349, 77
Collins, N. R., Kraemer, S. B., Crenshaw, D. M., et al. 2009, ApJ, 694, 765
Comerford, J. M., Negus, J., Barrows, R. S., et al. 2022, ApJ, 927, 23
Comerford, J. M., Negus, J., Müller-Sánchez, F., et al. 2020, ApJ, 901, 159
Comerford, J. M., Nevin, R., Stemo, A., et al. 2018, ApJ, 867, 66
Condon, J. J., Cotton, W. D., Greisen, E. W., et al. 1998, AJ, 115, 1693
Dasyra, K. M., Ho, L. C., Armus, L., et al. 2008, ApJL, 674, L9
Di Matteo, T., Springel, V., & Hernquist, L. 2005, Natur, 433, 604
Dodorico, S. 1978, MmSAI, 49, 485
Dodorico, S., Dopita, M. A., & Benvenuti, P. 1980, A&AS, 40, 67
Dopita, M. A. 1976, ApJ, 209, 395
Drory, N., MacDonald, N., Bershady, M. A., et al. 2015, AJ, 149, 77
Eisenstein, D. J., Weinberg, D. H., Agol, E., et al. 2011, AJ, 142, 72
Elitzur, M., & Shlosman, I. 2006, ApJL, 648, L101
Elmhamdi, A. 2011, AcA, 61, 179
Fabian, A. C. 2012, ARA&A, 50, 455
Farage, C. L., McGregor, P. J., Dopita, M. A., et al. 2010, ApJ, 724, 267
Ferguson, J. W., Korista, K. T., & Ferland, G. J. 1997, ApJS, 110, 287
Ferland, G. J., Korista, K. T., Verner, D. A., et al. 1998, PASP, 110, 761
Ferrarese, L., & Merritt, D. 2000, ApJL, 539, L9
Gebhardt, K., Bender, R., Bower, G., et al. 2000, ApJL, 539, L13
Gelbord, J. M., Mullaney, J. R., & Ward, M. J. 2009, MNRAS, 397, 172
Genzel, R., Lutz, D., Sturm, E., et al. 1998, ApJ, 498, 579
Glidden, A., Rose, M., Elvis, M., et al. 2016, ApJ, 824, 34

[9] http://www.astropy.org

Goulding, A. D., & Alexander, D. M. 2009, MNRAS, 398, 1165
Gunn, J. E., Siegmund, W. A., Mannery, E. J., et al. 2006, AJ, 131, 2332
Haardt, F., & Maraschi, L. 1991, ApJL, 380, L51
Haehnelt, M. G., Madau, P., Kudritzki, R., et al. 2001, ApJL, 549, L151
Heckman, T. M., & Best, P. N. 2014, ARA&A, 52, 589
Heckman, T. M., Kauffmann, G., Brinchmann, J., et al. 2004, ApJ, 613, 109
Hinkle, J. T., & Mushotzky, R. 2021, MNRAS, 506, 4960
Hopkins, P. F., Hernquist, L., Cox, T. J., et al. 2005, ApJ, 630, 705
Kewley, L. J., Dopita, M. A., Sutherland, R. S., et al. 2001, ApJ, 556, 121
Kewley, L. J., Groves, B., Kauffmann, G., & Heckman, T. 2006, MNRAS, 372, 961
Kormendy, J., & Ho, L. C. 2013, ARA&A, 51, 511
Kraemer, S. B., Trippe, M. L., Crenshaw, D. M., et al. 2009, ApJ, 698, 106
Laor, A. 2004, in ASP Conf. Ser. 311, AGN Physics with the Sloan Digital Sky Survey, ed. G. T. Richards & P. B. Hall (San Francisco, CA: ASP), 169
Law, D. R., Cherinka, B., Yan, R., et al. 2016, AJ, 152, 83
Lutz, D., Yan, L., Armus, L., et al. 2005, ApJL, 632, L13
Maoz, D., Nagar, N. M., Falcke, H., et al. 2005, ApJ, 625, 699
Mazzalay, X., Rodríguez-Ardila, A., & Komossa, S. 2010, MNRAS, 405, 1315
Molina, M., Reines, A. E., Latimer, L. J., et al. 2021, ApJ, 922, 155
Mullaney, J. R., Ward, M. J., Done, C., Ferland, G. J., & Schurch, N. 2009, MNRAS, 394, L16
Müller-Sánchez, F., Prieto, M. A., Hicks, E. K. S., et al. 2011, ApJ, 739, 69
Negus, J., Comerford, J. M., Müller Sánchez, F., et al. 2021, ApJ, 920, 62
Nevin, R., Blecha, L., Comerford, J., et al. 2019, ApJ, 872, 76
Newman, J. A., Cooper, M. C., Davis, M., et al. 2013, ApJS, 208, 5
O'Donnell, J. E. 1994, ApJ, 422, 158
Oh, K., Koss, M., Markwardt, C. B., et al. 2018, ApJS, 235, 4
Oh, K., Yi, S. K., Schawinski, K., et al. 2015, ApJS, 219, 1
Osterbrock, D. E. 1981, ApJ, 246, 696
Pennell, A., Runnoe, J. C., & Brotherton, M. S. 2017, MNRAS, 468, 1433
Penston, M. V., Fosbury, R. A. E., Boksenberg, A., Ward, M. J., & Wilson, A. S. 1984, MNRAS, 208, 347
Peterson, B. M. 1997, An Introduction to Active Galactic Nuclei (Cambridge: Cambridge Univ. Press)
Reefe, M., Satyapal, S., Sexton, R. O., et al. 2022, ApJ, 936, 140
Revalski, M., Crenshaw, D. M., Rafelski, M., et al. 2022, ApJ, 930, 14
Rich, J. A., Dopita, M. A., Kewley, L. J., et al. 2010, ApJ, 721, 505
Rich, J. A., Kewley, L. J., & Dopita, M. A. 2011, ApJ, 734, 87
Riffel, R. A., Bianchin, M., Riffel, R., et al. 2021, MNRAS, 503, 5161
Riffel, R. A., Dors, O. L., Armah, M., et al. 2021, MNRAS, 501, L54
Rodríguez-Ardila, A., Prieto, M. A., Portilla, J. G., et al. 2011, ApJ, 743, 100
Rodríguez-Ardila, A., Viegas, S. M., Pastoriza, M. G., et al. 2002, ApJ, 579, 214
Rose, M., Elvis, M., & Tadhunter, C. N. 2015, MNRAS, 448, 2900
Sajina, A., Lacy, M., & Pope, A. 2022, Univ, 8, 356
Satyapal, S., Kamal, L., Cann, J. M., et al. 2021, ApJ, 906, 35
Satyapal, S., Vega, D., Dudik, R. P., et al. 2008, ApJ, 677, 926
Schlegel, D. J., Finkbeiner, D. P., & Davis, M. 1998, ApJ, 500, 525
Seab, C. G., & Shull, J. M. 1983, ApJ, 275, 652
Smee, S. A., Gunn, J. E., Uomoto, A., et al. 2013, AJ, 146, 32
Smith, N., Silverman, J. M., Chornock, R., et al. 2009, ApJ, 695, 1334
Snow, T. P., & Witt, A. N. 1996, ApJL, 468, L65
Sturm, E., Lutz, D., Verma, A., et al. 2002, A&A, 393, 821
Sun, A.-L., Greene, J. E., & Zakamska, N. L. 2017, ApJ, 835, 222
Tadhunter, C. N., Fosbury, R. A. E., di Serego Alighieri, S., et al. 1988, MNRAS, 235, 403
Trindade Falcão, A., Kraemer, S. B., Crenshaw, D. M., et al. 2022, MNRAS, 511, 1420
Urry, C. M., & Padovani, P. 1995, PASP, 107, 803
Veilleux, S., & Osterbrock, D. E. 1987, ApJS, 63, 295
Voges, W., Aschenbach, B., Boller, T., et al. 1999, A&A, 349, 389
Voges, W., Aschenbach, B., Boller, T., et al. 2000, IAUC, 7432, 3
Wake, D. A., Bundy, K., Diamond-Stanic, A. M., et al. 2017, AJ, 154, 86
Weedman, D. W., Soifer, B. T., Hao, L., et al. 2006, ApJ, 651, 101
Westfall, K. B., Cappellari, M., Bershady, M. A., et al. 2019, AJ, 158, 231
Whysong, D., & Antonucci, R. 2004, ApJ, 602, 116
Willett, K. W., Lintott, C. J., Bamford, S. P., et al. 2013, MNRAS, 435, 2835
Wright, E. L., Eisenhardt, P. R. M., Mainzer, A. K., et al. 2010, AJ, 140, 1868
Wylezalek, D., Zakamska, N. L., Greene, J. E., et al. 2018, MNRAS, 474, 1499
Yan, R., & Blanton, M. R. 2012, ApJ, 747, 61
Yan, R., Bundy, K., Law, D. R., et al. 2016, AJ, 152, 197
York, D. G., Adelman, J., Anderson, J. E., et al. 2000, AJ, 120, 1579